An experimental study of the thermohydraulic characteristics of flow boiling in horizontal pipes: Linking spatiotemporally resolved and integral measurements

H.R. Moran[1], D. Zogg[1,2], V. Voulgaropoulos[1], W.J. Van den Bergh[3], J. Dirker[3], J.P. Meyer[3], O.K. Matar[3] and C.N. Markides[1,4,*]

This is the final accepted version of the manuscript, as first submitted to the journal.
The final published version can be found at:
`https://doi.org/10.1016/j.applthermaleng.2021.117085`

[1] *Department of Chemical Engineering, Imperial College London, London, U.K.*
[2] *Laboratory of Renewable Energy Science and Engineering, École Polytechnique Fédérale de Lausanne, Lausanne, Switzerland*
[3] *Department of Mechanical and Aeronautical Engineering, University of Pretoria, Pretoria, South Africa*
[4] *Kutateladze Institute of Thermophysics, Novosibirsk, Russian Federation*

[*] Corresponding author. Email: c.markides@imperial.ac.uk

Abstract

Data are presented from experiments of flow boiling in a horizontal pipe. Specifically, refrigerant R245fa was evaporated in a 12.6 mm stainless steel pipe to which a uniform heat flux of up to 38 kW/m^2 was applied. The bespoke facility operated at mass fluxes in the range 30-700 kg/m^2.s and a saturation pressure of 1.7 bar. Flow patterns were identified through high-speed imaging and the resulting flow pattern map is compared to existing maps in the literature. Predictive methods for the pressure drop and heat transfer coefficient from common correlations are also compared to the present experimental data, acting as verification of the facility and methods used for the macroscale boiling flows investigated in this work. Laser-induced fluorescence (for the identification of liquid phase) and particle image velocimetry (for the provision of velocity-field information) were also developed and successfully applied, providing detailed spatially- and temporally-resolved interfacial property, phase distribution and liquid-phase velocity-field data, alongside traditional integral pressure drop and overall heat transfer measurements. The laser-based methods provide new insight into the hydrodynamic and thermal characteristics of boiling flows at this scale, which are linked to the integral thermohydraulic data on flow regimes, pressure drops and heat transfer. This enhanced understanding can improve the design and operation of flow-boiling applications such as organic Rankine cycles and concentrating solar power facilities operation in the direct steam generation mode.

Keywords: flow boiling; flow pattern; heat transfer coefficient; laser diagnostics; pressure drop; two-phase flow

Nomenclature

Acronyms

2cLIF	two-colour laser-induced fluorescence
A	annular
CSP	concentrating solar power
DAQ	data acquisition device
DC	direct current
DSG	direct steam generation
FEP	fluorinated ethylene propylene
FLOBOF	flow boiling facility
I	intermittent
IR	infrared
LIF	laser-induced fluorescence
M	mist
MARD	mean absolute relative deviation
MRD	mean relative deviation
ORC	organic Rankine cycle
PIV	particle image velocimetry
PLIF	planar laser-induced fluorescence

PTV	particle tracking velocimetry
RI	refractive index
S	stratified
Slug+SW	slug plus stratified-wavy
SW	stratified-wavy

Latin symbols

A	area [m^2]
A_{LD}	dimensionless liquid cross-sectional area [-]
A_{VD}	dimensionless liquid cross-sectional area [-]
Bo	boiling number [-]
C	Ohmic correction constant [-]
Co	confinement number [-]
Cv	convection number [-]
c_p	heat capacity [J/kg.K]
d	diameter [m]
dp	pressure drop [Pa]
F	empirical coefficient [-]
Fr	Froude number [-]
h	heat transfer coefficient [W/m^2.K]
h_{LD}	dimensionless liquid height [-]
h_{lv}	latent heat of vaporisation [J/kg]
g	gravitational acceleration [m/s^2]
G	mass flux [kg/m^2.s]
I	current [A]
k	thermal conductivity [W/m.K]
L	length [m]
$\dot{m}$	mass flow rate [kg/s]
p	pressure [Pa]
P_{iD}	dimensionless liquid interface length
$\dot{q}$	heat flux [W/m^2]
$\dot{Q}$	heat transfer rate [W]
r	radius [m]

Re	Reynolds number [-]
T	temperature [K]
u	velocity [m/s]
V	voltage [V]
We	Weber number [-]
x	vapour quality [-]
X_{tt}	Lockhart Martinelli parameter [-]
y	vertical direction [m]
z	axial direction [m]

Greek symbols

ε	void fraction [-]
θ_{strat}	stratified angle [rad]
μ	viscosity [Pa.s]
ρ	density [kg/m^2]
σ	surface tension [N/m]
Φ	two-phase multiplier [-]

Subscripts

cb	convective boiling
exp	experimental
fric	frictional (pressure drop)
grav	gravitational
heated	heated
ht	heat transfer
i	inside
IA	intermittent to annular transition
int	interface
l	liquid
max	maximum
o	outside
nb	nucleate boiling
pipe	pipe
pred	predicted

sa	spatial acceleration
sat	saturation
strat	stratified
sc	subcooled
tp	two-phase
v	vapour
w	wall
wavy	stratified to stratified-wavy transition

1 Introduction

Boiling flows in horizontal pipes are present in evaporators, boilers and heat exchangers in a wide variety of applications. For example, refrigerants such as R245fa are used as the working fluid in organic Rankine cycle (ORC) systems for the generation of electrical power from low-temperature thermal energy sources [1, 2] such as solar heat [3, 4], or for waste heat recovery [5, 6]. Such fluids can also be used in high-temperature heat pumps, or in cooling and refrigeration systems. The understanding of boiling flows is also important for effective design and operation of concentrating solar power (CSP) plants operating in the direct steam generation (DSG) mode [7]. In this application, water boils directly inside the solar collector tube, rather than in a secondary circuit. As in all boiling flow applications, the development of a transient two-phase flow makes reliable control and operation of the system challenging, and creates a need for fundamental understanding of the hydrodynamic and heat transfer characteristics of these flows.

Many experimental studies have presented the investigation of boiling of various fluids in horizontal pipes of a wide range of diameters. However, there is a relative scarcity of data in pipe diameters above the 'mini' scale (i.e. $d > 3\,\mathrm{mm}$ [8]) for R245fa , which is currently one of the most dominant working fluids in ORC systems [9]. Therefore, validation of the many predictive methods available for flow pattern, pressure drop and heat transfer coefficient in these types of flows is required. The literature also lacks detailed spatiotemporally resolved information for these flows, including the interfacial dynamics, phase distribution and velocity fields. Experimental flow boiling data of this type of relevance to many heat transfer and heat recovery applications, such as those identified in the previous paragraph.

Two-phase flows are often characterised by their geometry and flow structure, the formation of which depends on the fluid properties, conditions, and phase fraction. Since the flow pattern can influence the pressure drop and heat transfer, it is essential to be able to predict the expected flow pattern regime under operation, for example according to transition lines plotted on a flow map. Kattan et al. [10] developed a two-phase flow pattern map for boiling in horizontal tubes with mass flux vs. vapour quality axes and transition lines calculated based on fluid properties and experimental conditions. They divided the map into five different flow patterns: 'stratified', 'stratified-wavy', 'intermittent', 'annular', and 'mist' flow. Wojtan et al. [11] later further divided the 'stratified-wavy' class, adding 'slug' as well as 'slug and stratified-wavy' flow patterns to the map. Various researchers have studied specific transition lines in more detail and proposed alternative [12, 13] or improved [14, 15] equations but a truly universal flow map for boiling is yet to be proposed due to the challenge of incorporating such a large number of intrinsically linked parameters.

Accurately predicting the pressure drop in boiling flows is key to the successful operation of many flow boiling applications. As such, various correlations exist for the calculation of two-phase frictional pressure drops, with the majority being separated flow models.

Lockhart and Martinelli [16] proposed the first separated flow model, but this does not accurately predict two-phase pressure drop and has been subsequently modified by many researchers. Grönnerud [17] expanded this approach further to specifically cover refrigerants, obtaining good results for some fluids and flows [18, 19], and his model was, in turn, modified by Friedel [20] based on a large experimental database. This extensive basis for the model means the Friedel [20] method is often found to be one of the most reliable for pressure-drop predictions over a wide range of conditions [21, 22]. Various authors have made further modifications to these correlations in order to improve their applicability to specific fluids and geometries (e.g. [23, 24]).

In another approach, the Müller-Steinhagen and Heck [25] method considers the frictional pressure gradients of both phases and performs an empirical interpolation between the two. This method has been found to perform well for a wide range of refrigerants [18] and other fluids [26], as well as across different pipe diameters [22, 23]. Mikielewicz [27] modified the Müller-Steinhagen and Heck [25] method for both flow boiling and condensation in minichannels by incorporating the surface tension effect to account for energy dissipation in the flow, and validated this new approach for refrigerants in 2.3 mm tubes [28].

Although not as widely developed or utilised due to their complexity, other predictive methods follow a phenomenological approach based on the flow pattern. Methods such as that of Quibén and Thome [29] utilise a flow pattern map (e.g. [11]) and formulate a pressure-drop calculation for each flow pattern separately. This way, interfacial phenomena can be accounted for through an interfacial friction factor which is calculated uniquely for each flow pattern.

The accurate prediction of heat transfer performance is vital for the design and subsequent operation of systems utilising flow boiling. Methods for predicting the two-phase heat transfer coefficient, h, in boiling flows typically consider the contributions of the two thermal mechanisms of nucleate boiling and convective boiling.

Some models employ an enhancement-factor approach, whereby h is based on the dominant heat transfer mechanism. An early example of this is the Shah [30] correlation which offered an improvement on that of Chen [31] for horizontal tubes and has been reported to give good predictions for R245fa boiling [32] and condensation [33]. Kandlikar [34] further developed the Shah [30] model, simplifying the implementation and modifying the nucleate to convective boiling transition criteria. This model is one of the most widely used enhancement-factor-type correlations, although various others have been developed more recently [35–37].

Gungor and Winterton [38] also developed a correlation based on the Chen [31] method, but accounted for both nucleate and convective boiling contributions in a superposition approach. Guo et al. [32] reported this to be the most accurate of eight common correlations when applied to R245fa boiling in a 10 mm inside diameter horizontal tube.

Liu and Winterton [39] were early adopters of an asymptotic approach using similar multipliers to Gungor and Winterton [38], whilst Steiner and Taborek [40] developed an asymptotic model for boiling in vertical tubes based on experimental data for a range of fluids. Some models have been developed for annular flow specifically [41, 42], and Guo et al. [43] modified the Liu and Winterton [39] correlation for boiling flows of R245fa and an R134a/R245fa mixture in smooth horizontal tubes of 3 mm inside diameter.

Other investigators have attempted to develop models valid for a wider range of conditions through a flow pattern-based approach. Kattan et al. [44] proposed one such model based on utilising their flow map [10] and the asymptotic heat transfer model of Steiner and Taborek [40]. Zürcher et al. [14] found this method to give accurate predictions when applied to the boiling of ammonia in horizontal tubes, but Wojtan et al. [11] proposed modifications based on their experimental data for boiling of R22 and R410A in horizontal tubes.

A further set of models calculate heat transfer coefficient based on considerations of energy dissipation. Mikielewicz and Mikielewicz [45] utilised their modified Müller-Steinhagen and Heck [25] two-phase multiplier to calculate heat transfer in minichannels.

They validated their new method against existing correlations and experimental data for flow condensation in the annular flow regime, in which they considered the phenomena to be symmetrical to that of flow boiling.

The applicability of flow boiling predictive methods to R245fa in truly macroscale pipe diameters (i.e. $d > 3\,\mathrm{mm}$) was investigated in this work, alongside advanced flow visualisation. In much of the flow boiling literature, flow visualisation has been mostly limited to the use of sight glasses and high-speed cameras to record images and videos for flow pattern identification [10, 46, 47]. Ursenbacher et al. [48] illuminated a cross-section of the flow with a laser sheet and recorded high-speed images from which they detected the vapour-liquid interface and thus extracted information on the dry angle and void fraction. Other than this, laser-based diagnostic techniques have not been widely applied to boiling flows, particularly under saturated boiling conditions. Estrada-Perez and Hassan [49] measured turbulence statistics of subcooled refrigerant flows in vertical channels using particle tracking velocimetry (PTV), and Hassan et al. [50] combined this measurement technique with infrared (IR) imaging to obtain temperature fields over the heated wall in similar geometries. Samaroo et al. [51] also used PTV to measure velocity profiles in vertical subcooled boiling flows, specifically investigating flow in an annulus. Particle image velocimetry (PIV) has been used in pool boiling experiments alongside IR thermometry [52] and two-colour laser-induced fluorescence (2cLIF) [53] to obtain corresponding temperature fields. However, detailed spatiotemporally resolved information in horizontal boiling flows is lacking.

In this work, following the work of Zadrazil and Markides [54], Charogiannis et al. [55] and Cherdantsev et al. [56], laser-diagnostic techniques based on PIV and LIF were developed and applied successfully to two-phase horizontal boiling flows in a macroscale pipe, specifically chosen to have a diameter that is larger than that typically investigated in earlier studies in the literature. The application of these techniques is important, as it enables us to generate spatiotemporal interface, phase and velocity distribution data, from which we can obtain new insight into key thermal and hydrodynamic characteristics of these flows. Such insights can be used to enhance the performance of flow boiling systems by identifying the most effective operating regimes and designing facilities accordingly.

The paper is organised as follows: in Section 2 a description of the experimental facility and data-collection procedures are presented, followed by a discussion of the results in

Section 3; finally, concluding remarks are made in Section 4.

2 Experimental methods

2.1 Experimental facility

Experimental measurements with the refrigerant R245fa as the test fluid have been performed using a bespoke Flow Boiling Facility, FLOBOF, comprising a flow circuit with a visualisation section for optical access. A simplified flow diagram of FLOBOF is shown in Figure 1. This work presents the first publication of experimental data from this facility.

In the refrigerant flow circuit, subcooled liquid is pumped from the bottom of a liquid receiver using a Crest AM50 TGARV centrifugal pump and passed to an Omega CHF081863 6 kW circulation heater used to preheat the liquid to the desired degree of subcooling at the test section inlet. The liquid is then passed through a 90 μm filter to protect the subsequent turbine flowmeter, the output of which is used to control the pump speed and regulate the flow rate into the test section. The 12.6 mm-inside diameter, 2 m-long stainless steel heated section is preceded by a 0.6 m-long flow calming and flow development section of the same material and inside diameter, which acts to eliminate entrance effects.

Fluid temperature, along with system pressure, is measured at the entrance to the heated section to determine the inlet conditions and again at the outlet. The liquid boils as it flows along the heated section, resulting in a two-phase vapour-liquid flow which enters the visualisation section. This section consists of a fluorinated ethylene propylene (FEP) pipe, of equal inside diameter to the stainless-steel heated section, encased in a perspex correction box filled with water. The fluid then flows through a water-cooled plate heat exchanger, in which the vapour condenses and the liquid is subcooled before being returned to the liquid receiver.

The output signals from the facility instrumentation were processed by three data acquisition devices (DAQs) and recorded through a LabView interface, which was also used for monitoring and control of the system. For a given set of experimental conditions, a steady-state was considered to be achieved when the instrument data remained within a 5 % range for at least 300 s, after which data was recorded for a period of 120 s.

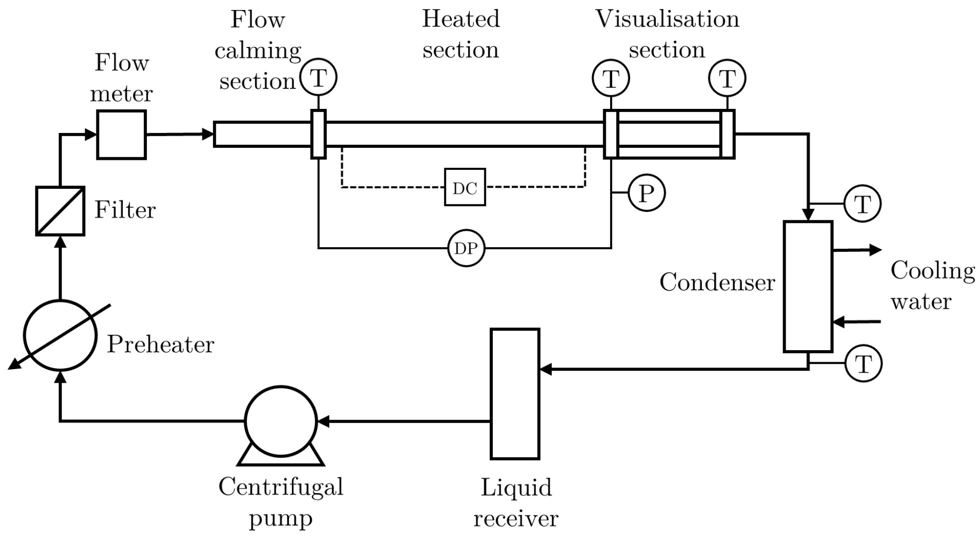

Figure 1: Flow diagram of the flow boiling facility (FLOBOF). Measurement locations for temperature, pressure and differential pressure are indicated by T, P and DP respectively.

2.1.1 Heated test section

The heated test section (see Fig. 2) comprises a stainless steel pipe with direct current (DC) heating, thermal insulation and measurement instrumentation. The pipe has an inside diameter, d_i, of 12.6 mm and length, L_ht, of 2 m and is connected to a Glassman Europe BPI 20 V, 750 A DC power supply via copper rods and braids to uniformly heat the surface of the pipe by application of direct current. The Ohmic losses in the rods and braids were checked and found to result in a 2 % loss of input power delivered to the pipe. The whole section is insulated with black nitrile rubber pipe insulation to a minimum thickness of 19 mm. Maximum heat losses of $< 1\,\%$ of input power were calculated across all experimental conditions by evaluating the single phase energy balance for a range of input powers and flowrates. FLOBOF was designed to investigate flow boiling starting from the subcooled liquid condition, as would be the case in industrial applications, and the test section is sufficiently long to investigate a range of outlet vapour qualities. As such, fluid enters the heated section as a subcooled liquid, is heated to saturation point, boils, and exits as a two-phase vapour-liquid flow with vapour quality x.

The pressure drop across the heated test section was measured using two Rosemount differential pressure transmitters with a zero-order measurement uncertainty of ± 0.1 % of the calibrated range, set to 0–5 kPa and 0–20 kPa for the two instruments. The absolute pressure at the outlet was measured using an Omega PXM309 pressure transmitter with a zero-order measurement uncertainty of ± 1 %. The combination of the absolute and

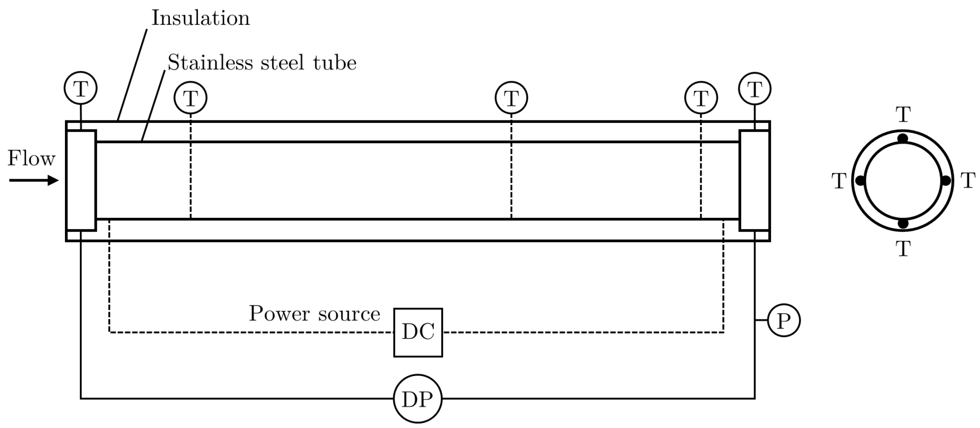

Figure 2: Schematic of the heated test section. Measurement locations for temperature, pressure and differential pressure are indicated by T, P and DP respectively.

differential pressure measurements allowed calculation of the pressure at the inlet to the heated section. The inlet and outlet temperatures were measured using in-flow mineral insulated T-type thermocouples of 0.5 mm diameter. The wall temperature was measured using 0.38 mm diameter bead-welded T-type thermocouples, electrically insulated from the live pipe wall by a thin layer of polyimide film to which the thermocouples are attached with thermally conductive epoxy glue. The thermocouple wires are encased in electrically insulating sheaths then passed along the pipe wall inside the insulation to minimise conduction errors. Wall thermocouples are placed at three measurement junctions 0.125 m, 1.575 m and 1.875 m from the inlet, with thermocouples placed at 90° intervals around the pipe circumference, as shown in Fig. 2.

All of the thermocouples in the facility, including those for in-flow and wall temperature measurements, were calibrated against a digital reference thermometer certified with a 5-point UKAS calibration in a thermal bath to an average accuracy of 0.25 K. The mean absolute difference in temperature between the two lateral wall thermocouples at each measurement junction was 0.19 K, which is within the experimental uncertainty and therefore indicates a satisfactory temperature measurement. The differential pressure transmitters were calibrated *in situ* using a Fluke709H HARTmeter.

2.1.2 Visualisation section

To allow optical access, a visualisation section was constructed at the outlet of the heated test section. An effective visualisation section for application of any optical diagnostic technique to two-phase pipe flows should be designed to minimise optical distortions due to the refraction of light at all fluid-fluid and fluid-solid interfaces, and this is ideally achieved with a fully refractive index (RI) matched system [57]. However, this is highly challenging in a boiling flow since the two fluid phases have very different RIs, and additionally liquid R245fa has a low RI (1.25 at 20 °C). As such, an FEP pipe, of equal inside diameter to the heated test section, was used for the visualisation section. FEP has a low RI compared to other suitable optically accessible pipe materials and is translucent. The FEP pipe is encased in a correction box constructed from acrylic and filled with distilled water, the RI of which is within 1 % of that of the FEP pipe across the range of operating conditions. This box reduces optical distortion due to the curvature of the pipe and relative position of the camera.

For simple visualisation of the flow through high-speed imaging, and for flow pattern identification, a backlight and camera were positioned as shown in Fig. 3a. The camera used was an Olympus iSpeed 3 with a maximum resolution of 1280 by 1024 pixels at a maximum frame rate of 2 kHz, equipped with a Sigma 105 mm lens and installed in a horizontal orientation perpendicular to the correction box.

For the laser-based measurements, the flow was illuminated by a laser sheet generated by a copper vapour laser that emits two narrow band laser beams at 510.6 nm (green light) and 578.2 nm (yellow light) at a nominal output power of 20 W, frequency of 2 kHz, pulse-duration of 2 ns, and pulse energy of 2 mJ. The beams were directed to a sheet generator via a fibre-optic cable, with the sheet expanded in the streamwise direction and illuminating the flow in a plane through the (axial) centreline of the pipe from the bottom of the correction box. The liquid phase flow was seeded with 10 µm silver-coated reflective particles to enable particle image velocimetry (PIV) and with the fluorescent dye Rhodamine 6G at a concentration of 1 ppm to allow laser-induced fluorescence (LIF) measurements. The same iSpeed 3 high-speed camera was used to capture instantaneous images of the flow. In this application, the camera was mounted at an angle of approximately 20° from the horizontal and fitted with a corrective Scheimpflug filter. The camera captured both the scattered light from the particles (for PIV) and the fluorescent emission from the dye (for PLIF) in the liquid phase.

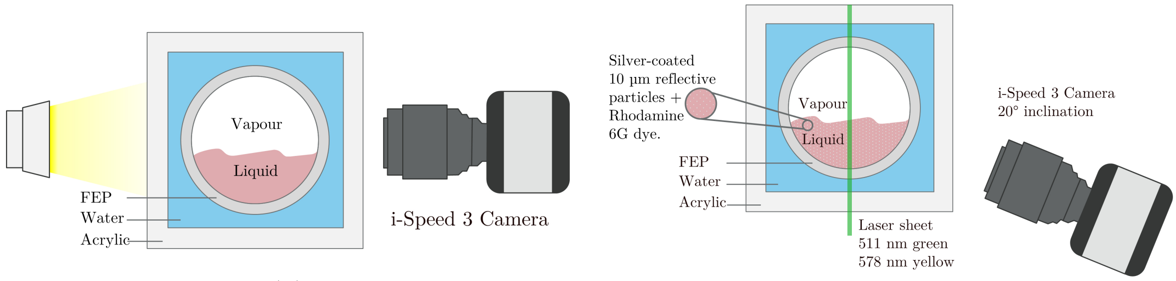

(a) (b)

Figure 3: Camera arrangement for: (a) qualitative flow visualisation, and (b) laser-based measurements.

2.1.3 Image processing

To obtain meaningful quantitative information from high-speed imaging of the laser-sheet-illuminated flows, extensive image processing was required. Images were recorded at a frame rate of 1500–2000 fps, with images recorded for a duration of at least 6.5 s for each flow condition to ensure statistical significance of the results. The image processing was undertaken using a combination of the *DaVis* software by LaVision and MATLAB algorithms developed in-house. After a preprocessing step, two strands of image analysis were undertaken; interface detection and velocity field identification. The detailed steps in these processes were as follows:

1. First, the images were loaded into the *DaVis* software and a spatial correction was applied based on calibration images obtained of a grid of known dimensions inserted into the liquid-filled pipe. This procedure corrected for the distortion induced by the angle of the camera (see Fig. 3b), and facilitated scaling of the images. The images were also rotated slightly to ensure alignment to the horizontal and mirrored around the vertical to give a flow direction of left-to-right.

2. The images obtained in *DaVis* were then loaded into MATLAB using LaVision's *Readimx* add-on. An algorithm was developed to identify the vapour-liquid interface comprising the following steps for each image:

   (a) First, the image was cropped to the region of interest to remove the area outside of the pipe walls and any dead space introduced from the calibration. The remaining image had a height equal to the pipe inside diameter, d_i, and a width of approximately $2d_\mathrm{i}$ in the direction of flow.

(b) An adaptive threshold was applied to the cropped image based on the local median at each pixel with a window size of 7 px. This removed the intensity hotspots of the particles and increased the intensity difference between the vapour and liquid phases.

(c) The image was binarised using the *imbinarize* function with an adaptive thresholding approach, a sensitivity of 0.5 and the classification of a bright foreground. An area filter was then applied to the resulting black and white image to extract only the largest structures thereby removing any residual light areas due to particles.

(d) The interface was identified by locating the point in the black and white image matrix at which a step change occurred. Any unphysical spikes in the interface were removed and the interface was smoothed using a Savitsky-Golay filter.

(e) A mask was created based on the interface location, with areas under the vapour-liquid interface (i.e. the liquid phase) assigned a value of 1 and any other areas assigned a NaN value.

3. Velocity fields were extracted from the spatially corrected images obtained in step 1 using the following method:

   (a) In *DaVis*, the 'Subtract sliding average' processing step was applied to subtract a 2D sliding average with a 5 px filter length based on a Gaussian profile. This enhanced the intensity difference between the particles and the liquid making them easier to identify in the following step.

   (b) PIV vectors were calculated using the functionality in *DaVis* taking a multipass approach with a decreasing window size from 96 by 96 to 32 by 32. The particle patterns were tracked between temporally adjacent images and the velocity field inferred with a spatial resolution of 8 px, or 0.16 mm.

   (c) The resulting vector field was loaded into MATLAB using the *pivmat* toolbox and multiplied by the mask generated in step 2(e). This masking was applied after generating the velocity fields to ensure that the velocity field close to the interface was adequately captured.

This image processing approach follows conventional techniques similar to those described in further detail by Charogiannis et al. [55] and Ibarra et al. [58].

2.2 Data reduction

The raw data obtained from the heated test section described in Section 2.1.1 required some treatment to provide the set of integral measurements common in the flow boiling literature. The data reduction process applied to the raw data is described in this section.

The pressure drop measured experimentally, $\mathrm{d}p_{\mathrm{exp}}$, was the total pressure drop and therefore the sum of the gravitational, frictional, and spatial acceleration pressure drops as follows:

$$\mathrm{d}p_{\mathrm{exp}} = \mathrm{d}p_{\mathrm{grav}} + \mathrm{d}p_{\mathrm{fric}} + \mathrm{d}p_{\mathrm{sa}} \tag{1}$$

Since the flow was horizontal, $\mathrm{d}p_{\mathrm{grav}} = 0$. Two-phase pressure drop predictive methods in the literature calculate the frictional pressure drop, so the spatial acceleration pressure drop was calculated according to the method of Collier and Thome [59] as follows:

$$\mathrm{d}p_{\mathrm{sa}} = G^2 \left\{ \left[\frac{(1-x)^2}{(1-\varepsilon)\rho_{\mathrm{l}}} + \frac{x^2}{\varepsilon \rho_{\mathrm{v}}} \right]_{\mathrm{out}} - \left[\frac{(1-x)^2}{(1-\varepsilon)\rho_{\mathrm{l}}} + \frac{x^2}{\varepsilon \rho_{\mathrm{v}}} \right]_{\mathrm{in}} \right\} \tag{2}$$

where ε is the void fraction calculated using the Steiner [60] formulation of the Rouhani and Axelsson [61] drift flux void fraction correlation; G is the mass flux, and ρ_l and ρ_V denote the densities of the liquid and vapour phases, respectively.

The experimental heat transfer coefficient h was calculated as follows:

$$h = \frac{\dot{Q}_{\mathrm{in}}}{A_{\mathrm{ht}}(T_{\mathrm{w,i}} - T_{\mathrm{sat}})} \tag{3}$$

where $\dot{Q}_{\mathrm{in}}$ is the heat input rate based on the input voltage, V, and current, I, of the power supply such that $\dot{Q}_{\mathrm{in}} = VI \times C$, where C is a constant that corrects for Ohmic (resistive) losses in the copper rods and braids connecting the power supply to the test section. A_{ht} is the heat transfer surface area to the fluid, $A_{\mathrm{ht}} = \pi d_{\mathrm{i}} L_{\mathrm{ht}}$. $T_{\mathrm{w,i}}$ is the inside wall temperature and T_{sat} is the saturation temperature of the fluid evaluated at the known saturation pressure.

The inside wall temperature, $T_{\mathrm{w,i}}$, was calculated from the outside wall temperature, $T_{\mathrm{w,o}}$, by solving a one-dimensional conduction equation across the pipe wall, assuming uniform heat generation in an isotropic and homogeneous material:

$$T_{\mathrm{w,i}} = T_{\mathrm{w,o}} + \frac{\dot{Q}_{\mathrm{in}}}{2\pi k_{\mathrm{pipe}} L_{\mathrm{ht}} (r_{\mathrm{o}}^2 - r_{\mathrm{i}}^2)} \left(\frac{r_{\mathrm{o}}^2 - r_{\mathrm{i}}^2}{2} + r_{\mathrm{o}}^2 \ln \frac{r_{\mathrm{i}}}{r_{\mathrm{o}}} \right) \tag{4}$$

where $k_{\text{pipe}} = 16.3$ W/m.K is the thermal conductivity of the stainless steel pipe and r_{i} and r_{o} are its inner and outer radii respectively.

The inside wall temperature and corresponding heat transfer coefficient were calculated for each wall thermocouple location, then a spatially averaged h calculated at each thermocouple junction from the four local h values. The vapour quality, x, was calculated by performing a heat balance across the heated test section:

$$x = \frac{\dot{Q}_{\text{in}} - \dot{m} c_p \Delta T_{\text{sc}}}{\dot{m} h_{\text{lv}}} \tag{5}$$

where $\dot{m}$ is the mass flow rate in kg/s, c_p is the liquid heat capacity at inlet conditions, ΔT_{sc} is the degree of subcooling at the pipe inlet, i.e. $\Delta T_{\text{sc}} = T_{\text{sat,in}} - T_{\text{in}}$ and h_{lv} is the latent heat of vaporisation of the liquid. x was calculated at the outlet of the heated test section, and at the location of each thermocouple junction with $\dot{Q}_{\text{in}}$ scaled according to the corresponding heated length.

All thermophysical fluid properties were calculated at the relevant conditions using CoolProp [62].

When assessing the accuracy of predictive methods, the mean relative deviation (MRD) and mean absolute relative deviation (MARD) of a variable X were calculated as:

$$\text{MRD} = \frac{1}{n} \sum_{i=1}^{n} \frac{X_{\text{pred}} - X_{\text{exp}}}{X_{\text{exp}}} \tag{6}$$

$$\text{MARD} = \frac{1}{n} \sum_{i=1}^{n} \left| \frac{X_{\text{pred}} - X_{\text{exp}}}{X_{\text{exp}}} \right| \tag{7}$$

2.3 System verification and error analysis

To validate the performance of the FLOBOF system and measurement instruments, experiments were performed with single phase liquid R245fa flow under both adiabatic and heated conditions, with care taken to monitor the visualisation section for the appearance of bubbles that would indicate the onset of boiling and invalidate the single phase tests. The resulting Nusselt numbers were compared to those calculated using the Meyer et al. [63] correlations to within an average deviation of 7 %. The pressure drop data were compared to the Fang et al. [64] correlation with an average deviation of 8 %. The mean deviations for both values are well within 10 % and the facility can be considered validated.

Table 2: Experimental uncertainties

Parameter	Uncertainty
$T_{\mathrm{w,o}}$	0.3 K
T_{fluid}	0.3 K
G	8.8 %
$\dot{q}$	1.8 % to 6.6 %
h	6.0 % to 23 %
x	0.0085
p	2.2 %
dp	0.1 % to 6.1 %

The overall experimental uncertainty in integral measurements was evaluated using the method proposed by Moffat [65] and the resulting values are reported in Table 2. These uncertainty values account for the error in the measurement instruments themselves, along with all data processing and conversion steps and a consideration of the time-dependent variance of each measurement, given that the reported values have been temporally averaged.

The experimental uncertainty in laser-based measured measurements was evaluated based on the image resolution and standard deviation of the calculated values. The interface height has a mean uncertainty of ± 0.16 mm, whilst the liquid-phase velocity obtained using PIV has a mean uncertainty of ± 35 %.

3 Results and discussion

3.1 Flow patterns

High-speed images were recorded for various flow patterns, and some representative examples are shown in Fig. 4. The selected images demonstrate the characteristic features of the various flow regimes: a smooth, flat interface in stratified (S) flow with two continuous phases; the same two phases present in stratified-wavy (SW) flow but with a perturbed interface; a continuous liquid phase interrupted by elongated vapour bubbles in slug flow,

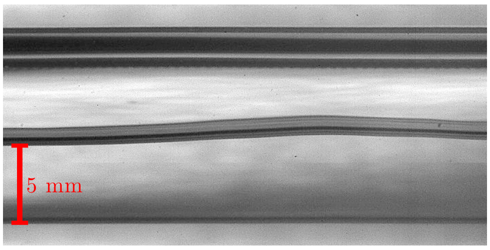

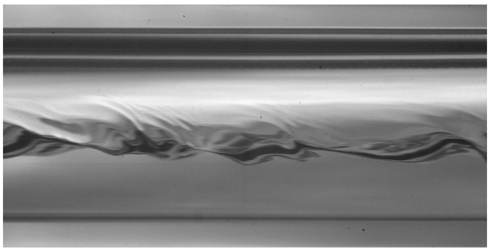

(a) Stratified (S)

$G = 50$ kg/m^2.s, $\dot{q} = 0.5\,$kW/m^2

(b) Stratified-wavy (SW)

$G = 68$ kg/m^2.s, $\dot{q} = 2.3\,$kW/m^2

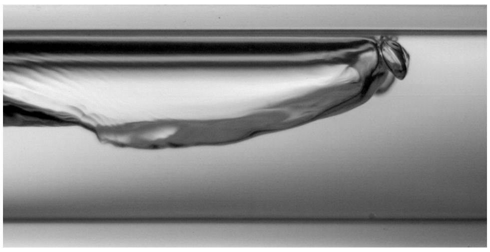

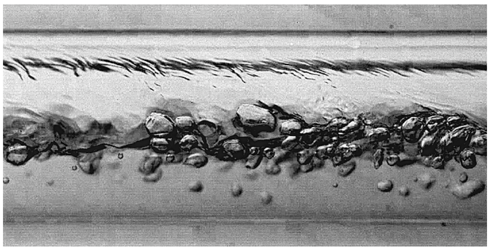

(c) Slug

$G = 173$ kg/m^2.s, $\dot{q} = 2.3\,$kW/m^2

(d) Intermittent (I)

$G = 390$ kg/m^2.s, $\dot{q} = 9.3\,$kW/m^2

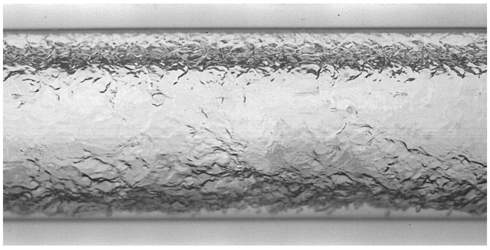

(e) Annular (A)

$G = 422$ kg/m^2.s, $\dot{q} = 38\,$kW/m^2

Figure 4: Flow patterns captured in FLOBOF using high-speed imaging.

with the liquid film maintained at the top of the vapour bubble; a liquid film on the pipe walls in annular (A) flow with ripples at the vapour/liquid interface; and a combination of a number of these characteristics in intermittent (I) flow. Mist (M) and dryout (D) flows were not captured in FLOBOF due to the high heat and mass fluxes required, and the unstable behaviour of the facility at high x due to the large vapour volumes present in the system. The high-speed images were captured at 1500 fps and were used to identify flow patterns according to the classifications put forward by Wojtan et al. [11] for a range of experimental conditions covering the parameter space $G = 30$-700 kg/m^2.s, $\dot{q} = 0.5$–$38\,$kW/m^2.

In this section, the experimental data collected over the full range of conditions are plotted together on single flow maps to facilitate visualisation. However, flow map transition lines, such as those proposed by Wojtan et al. [11], should in reality be plotted for each data point if one wishes to accurately determine the flow pattern, since their position can be dependent on the unique experimental parameters (x, G, $\dot{q}$, T_{sat}). The transition lines most affected by these parameters are the A/SW to D and D to M transitions, which were not relevant for this data set. For the range of experimental conditions studied, the other transitions lines vary by a maximum of approximately 20 %.

The most common flow map configuration in the modern flow boiling literature is that of G vs. x. The data points collected in FLOBOF are presented in Fig. 5, where an alternative presentation with a logarithmic x is provided as an inset to show the region $x < 0.1$ in more detail. The resulting map shows clearly the limitations of the facility, with data points at both high x and G not possible to obtain, making the dryout and mist regimes inaccessible. The facility also does not allow for data collection at high x and low G, since the resulting vapour volumes destabilise its operation by inducing slugging within the system. Figure 5 shows clear regions for Slug, I, and A flows, with some overlap of the S, SW and Slug+SW regimes. Stratified flow occurs at low G and low x, but as x increases the interface becomes less stable and a stratified wavy flow is observed. As G increases the vapour phase is no longer continuous and the flow moves into the Slug+SW and Slug regimes. At higher values of x, the mass flow rate of vapour increases and intermittent, then annular flows can be observed.

In Fig. 6, the experimental data points are plotted along with the Wojtan et al. [11] transition lines calculated for the conditions $\dot{q} = 14\,\mathrm{kW/m^2}$, $G = 332$ kg/m^2.s, $p_{\mathrm{sat}} = 1.7\,\mathrm{bar}$, which are representative of the data set as a mean. The calculation procedure for these transition lines according to Wojtan et al. [11] begins with calculating the geometrical parameters ε, A_{LD}, A_{VD}, θ_{strat}, h_{LD} and P_{iD}. ε is the void fraction calculated using the Steiner [60] formulation of the Rouhani and Axelsson [61] drift flux void fraction correlation, as mentioned in Section 2. The dimensionless liquid and vapour cross sectional areas, A_{LD} and A_{VD}, are defined based on the cross-sectional area of the heated section, A, as:

$$A_{\mathrm{LD}} = \frac{A(1-\varepsilon)}{d_{\mathrm{i}}^2}; \qquad A_{\mathrm{VD}} = \frac{A\varepsilon}{d_{\mathrm{i}}^2} \tag{8}$$

The dimensionless liquid height h_{LD} and dimensionless liquid interface length P_{iD} are expressed as a function of the stratified angle θ_{strat}, which can be calculated using an approximation proposed by Biberg [66] in terms of ε to avoid the need for solution by

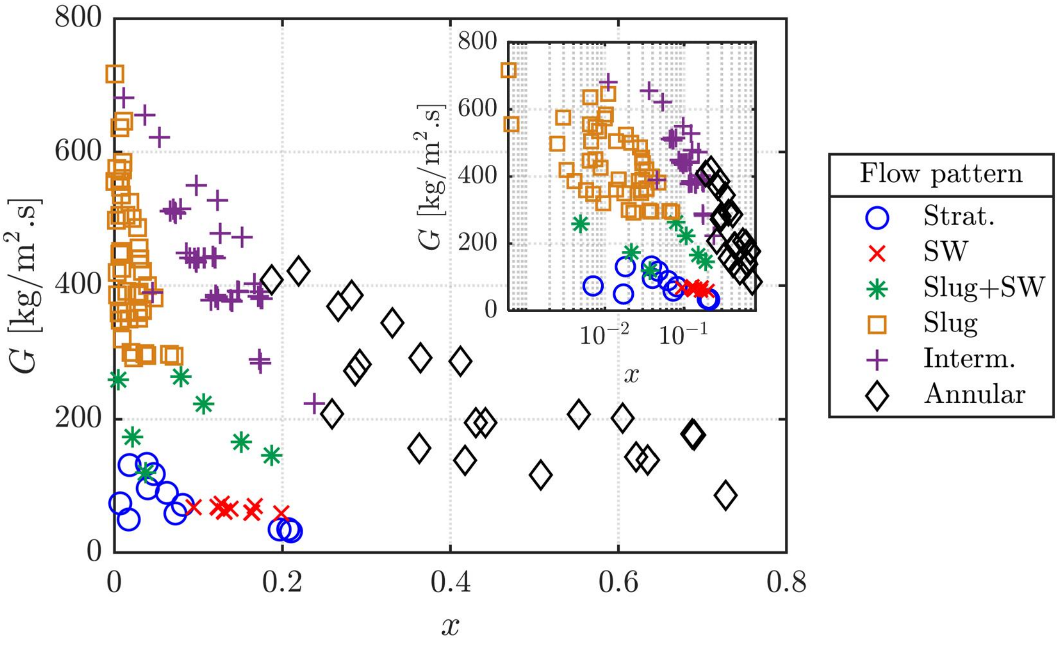

Figure 5: Flow pattern map with G vs x axes summarising all experimental data points for $p_{\mathrm{sat}} = 1.7\,\mathrm{bar}$, with inset showing a logarithmic x-axis for better visualisation at low x. The experimental uncertainties for G and x are $\pm 8.8\,\%$ and ± 0.0085 respectively.

iteration.

$$h_{\mathrm{LD}} = 0.5\left(1 - \cos\left(\frac{2\pi - \theta_{\mathrm{strat}}}{2}\right)\right) \tag{9}$$

$$P_{\mathrm{iD}} = \sin\left(\frac{2\pi - \theta_{\mathrm{strat}}}{2}\right) \tag{10}$$

$$\theta_{\mathrm{strat}} = 2\pi - 2\left\{\begin{array}{c} \pi(1-\varepsilon) + \left(\frac{3\pi}{2}\right)^{1/3}\left[1 - 2(1-\varepsilon) + (1-\varepsilon)^{1/3} - \varepsilon^{1/3}\right] \\ -\frac{1}{200}(1-\varepsilon)\varepsilon[1-2(1-\varepsilon)][1+4((1-\varepsilon)^2+\varepsilon^2)] \end{array}\right\} \tag{11}$$

The vertical I to A boundary is generally assumed to occur at a fixed value of the Martinelli parameter, $X_{\mathrm{tt}} = \left(\frac{1-x}{x}\right)^{0.875}\left(\frac{\rho_{\mathrm{v}}}{\rho_{\mathrm{l}}}\right)^{0.5}\left(\frac{\mu_{\mathrm{l}}}{\mu_{\mathrm{v}}}\right)^{0.125} = 0.34$, which is solved to give the corresponding vapour quality x_{IA}.

The SW to I/A transition line is calculated using the equation proposed by Kattan et al. [10] as follows:

$$G_{\mathrm{wavy}} = \left\{\frac{16A_{\mathrm{VD}}^3 g d_{\mathrm{i}} \rho_{\mathrm{l}} \rho_{\mathrm{v}}}{x^2\pi^2(1-(2h_{\mathrm{LD}}-1)^2)^{0.5}}\left[\frac{\pi^2}{25h_{\mathrm{LD}}^2}\left(\frac{\mathrm{We}}{\mathrm{Fr}}\right)_{\mathrm{l}}^{-1} + 1\right]\right\}^{0.5} + 50 \tag{12}$$

where the ratio of the liquid Weber and Froude numbers is calculated as $(\mathrm{We}/\mathrm{Fr})_{\mathrm{l}} = g d_{\mathrm{i}}^2 \rho_{\mathrm{l}}/\sigma$, σ is the surface tension. Wojtan et al. [11] then divided the SW area under this line into three regions such that:

- The Slug region is defined as $G > G_{\mathrm{wavy}}(x_{\mathrm{IA}})$;
- The Slug+SW region meets the criteria $G_{\mathrm{strat}} < G < G_{\mathrm{wavy}}(x_{\mathrm{IA}})$ and $x < x_{\mathrm{IA}}$;
- The SW region is then given by $x \geq x_{\mathrm{IA}}$.

The S to SW transition line is calculated using the equation proposed by Kattan et al. [10]:

$$G_{\mathrm{strat}} = \left\{ \frac{226.3^2 A_{\mathrm{LD}} A_{\mathrm{VD}}^2 \rho_{\mathrm{v}} (\rho_{\mathrm{l}} - \rho_{\mathrm{v}}) \mu_{\mathrm{l}} g}{x^2 (1-x) \pi^3} \right\}^{1/3} \tag{13}$$

with the additional condition that $G_{\mathrm{strat}} = G_{\mathrm{strat}}(x_{\mathrm{IA}})$ at $x < x_{\mathrm{IA}}$.

The equations of the A to D and D to M transition lines are not included here since they are not relevant to this work.

The Wojtan et al. [11] transition lines describe the data reasonably well with the flow pattern correctly predicted for 79 % of data points. The majority of the incorrectly predicted flow patterns occur in the Slug+SW, SW and S regimes below the transition curve to the I and A regimes (G_{wavy}), with some more occurring at the I to A transition line (x_{IA}). Wojtan et al. [11] divided the region between the G_{strat} and G_{wavy} curves into Slug, Slug+SW and SW, a modification to the earlier version of this map, by Kattan et al. [10]. The three different flow patterns were clearly observed experimentally, but alternative transition boundaries to those of Wojtan et al. [11] may be more appropriate for R245fa based on the lack of alignment with experimental data points in Fig. 6. Wojtan et al. [11] also modified the Kattan et al. [10] S to SW/Slug+SW transition curve (G_{strat}), assigning a constant value to G_{strat} at $x < x_{\mathrm{IA}}$. This does not fit the data well in this case, and it should be noted that Wojtan et al. [11] did not observe any stratified flow in their experiments, so the transition curve bounding the stratified region is not validated. For R245fa boiling at these conditions, it may also be appropriate to shift the I to A transition line to a smaller value of x_{IA}, although more data are required to validate this. Detailed laser-based measurements of the interface location could be used to improve the predictions of A_{LD}, θ_{strat} and P_{iD} in the Wojtan et al. [11] method for the stratified family of flow patterns.

Zürcher et al. [14] investigated the application of the Kattan et al. [10] flow map to ammonia boiling in a 14 mm ID horizontal tube. They proposed empirical corrections to the G_{strat} transition curve, which was observed to be too low, and the G_{wavy} transition curve, which was observed to be too high at high vapour qualities. Like Kattan et al. [10],

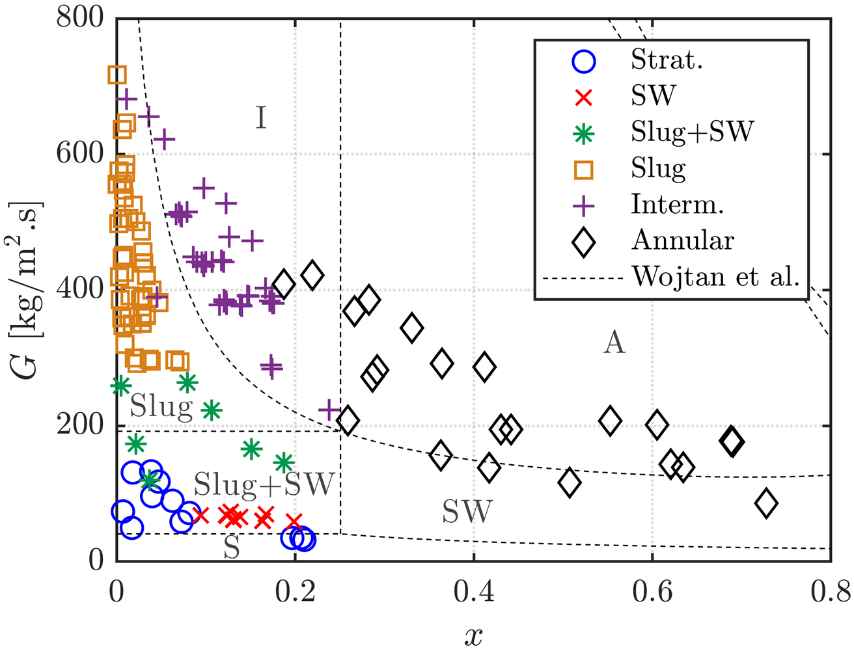

Figure 6: Flow pattern map summarising all experimental data points, $p_{\text{sat}} = 1.7\,\text{bar}$, with transition lines and flow pattern regions according to method of Wojtan et al. [11] for the conditions $\dot{q} = 14\,\text{kW/m}^2$, $G = 332$ kg/m^2.s.

they also grouped the Slug+SW and Slug flow patterns into one section of the map, and SW and S flow patterns into another section. The modified Zürcher et al. [14] transition lines are calculated as follows for horizontal tubes:

$$G_{\text{strat}} = \left\{ \frac{226.3^2 A_{\text{LD}} A_{\text{VD}}^2 \rho_{\text{v}} (\rho_{\text{l}} - \rho_{\text{v}}) \mu_{\text{l}} g}{x^2 (1-x) \pi^3} \right\}^{1/3} + 20x \tag{14}$$

$$G_{\text{wavy}} = \left\{ \frac{16 A_{\text{VD}}^3 g d_{\text{i}} \rho_{\text{l}} \rho_{\text{v}}}{x^2 \pi^2 (1 - (2h_{\text{LD}} - 1)^2)^{0.5}} \left[\frac{\pi^2}{25 h_{\text{LD}}^2} (1-x)^{F_1} \left(\frac{\text{We}}{\text{Fr}} \right)_{\text{l}}^{F_2} + 1 \right] \right\}^{0.5} + 50 - 75 e^{-[(x^2 - 0.97)^2 / x(1-x)]} \tag{15}$$

where the parameters F_1 and F_2 are empirical coefficients that account for the effect on heat flux on dryout.

The Zürcher et al. [14] G_{strat} line, as plotted in Fig. 7, does appear to give a better match to the experimental data. Note that the $\dot{q}$ dependence is mostly expressed in the part of the curve at high x, i.e. the dryout region, but that is not of interest since these conditions cannot be reached with the current experimental setup. The G_{wavy} line also encompasses the data slightly better than that of the Wojtan et al. [11] map , since it returns a lower value of G_{wavy} at intermediate x.

It can also be useful to consider specifically the transition from slug/bubble based flow

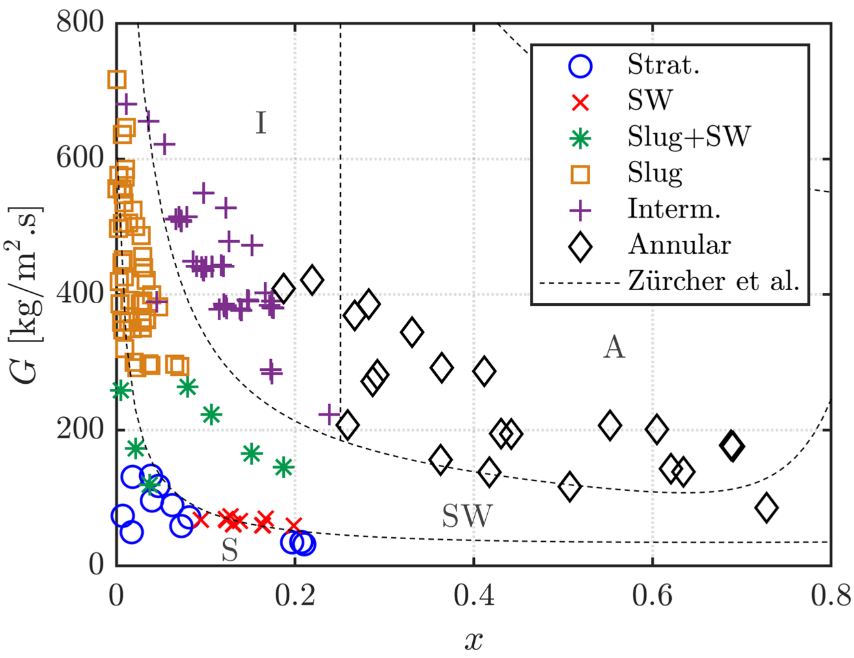

Figure 7: Flow pattern map summarising all experimental data points, $p_{\mathrm{sat}} = 1.7\,\mathrm{bar}$, with transition lines and flow pattern regions according to method of Zürcher et al. [14] for the conditions $\dot{q} = 14\,\mathrm{kW/m^2}$, $G = 332$ kg/m^2.s.

to annular/intermittent type flows, i.e. the G_{wavy} transition line. Figure 8 shows three such transition lines (those of Wojtan et al. [11], Ong and Thome [12], Costa-Patry and Thome [13]) plotted for the experimental conditions. More of the I/A data points are correctly situated on the flow map for both the Ong and Thome [12] and Costa-Patry and Thome [13] transition lines, the calculation of both of which involves the confinement number $\mathrm{Co} = (1/d_{\mathrm{i}}) \cdot \sqrt{\sigma/(g(\rho_{\mathrm{L}} - \rho_{\mathrm{V}}))}$. Ong and Thome [12] defined the transition line as:

$$x_{\mathrm{wavy}} = 0.047\mathrm{Co}^{0.05} \left(\frac{\mu_{\mathrm{v}}}{\mu_{\mathrm{l}}}\right)^{0.7} \left(\frac{\rho_{\mathrm{v}}}{\rho_{\mathrm{l}}}\right)^{0.6} \frac{\mathrm{Re_v}^{0.8}}{\mathrm{We_l}^{0.91}} \tag{16}$$

whilst Costa-Patry and Thome [13] proposed the equation:

$$x_{\mathrm{wavy}} = 425 \left(\frac{\rho_{\mathrm{v}}}{\rho_{\mathrm{l}}}\right)^{0.1} \frac{\mathrm{Bo}^{1.1}}{\mathrm{Co}^{0.5}} \tag{17}$$

where the boiling number is defined as $\mathrm{Bo} = \dot{q}/(h_{\mathrm{lv}} G)$.

The Barbieri et al. [15] transition line in Fig. 8 presents an alternative I-to-A transition to the fixed value of x_{IA} used by Wojtan et al. [11], given by:

$$G_{\mathrm{IA}} = \frac{(3.75 X_{\mathrm{tt}}^{2.40} \rho_{\mathrm{l}}^2 g d_{\mathrm{i}})^{0.5}}{(1 - x)} \tag{18}$$

The position of the experimental data points on the flow pattern map suggests that a transition curve of this type may be more appropriate, but the Barbieri et al. [15]

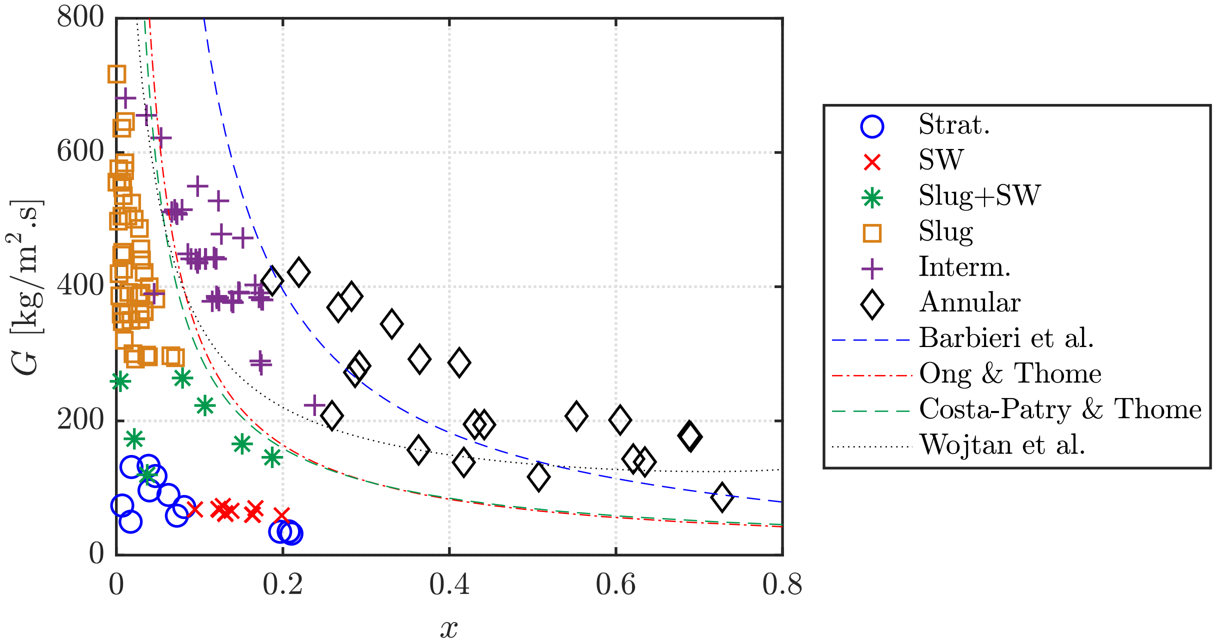

Figure 8: Flow pattern map summarising all experimental data points and a range of transition curves, $p_{\mathrm{sat}} = 1.7\,\mathrm{bar}$. The Costa-Patry and Thome [13] curve is generated for $\dot{q} = 14\,\mathrm{kW/m^2}$.

curve does not fit the data well. The calculation is not dependent on $\dot{q}$, so the differing $\dot{q}$-conditions of the data points cannot account for this deviation. Instead, tuning of the empirical coefficients is required, since the Barbieri et al. [15] transition curve was developed for R-134a in a brass tube and may not apply to different fluids and pipe materials.

3.2 Comparisons with pressure drop predictions

Experimental pressure drops were measured for 142 experimental data points with the parameter ranges G = 30–700 kg/m^2.s, $\dot{q}$ = 0.5–38 kW/m^2. In the setup shown in Figs. 1 and 2, the fluid always entered the measurement section as a subcooled liquid, and exited with a vapour quality, x, of up to 0.73. The reported results correspond to average values over the sample time during which the measurement was steady according to the procedure described in Section 2.1.

Many correlations for the prediction of frictional two-phase pressure drop ($\mathrm{d}p_{\mathrm{fric}}$) of boiling flows are available in the literature, but the application of these methods to R245fa boiling in macroscale tubes (i.e. $d_{\mathrm{i}} > 6\,\mathrm{mm}$) is not well documented. A few methods that perform well for similar experimental set-ups were selected and are compared to

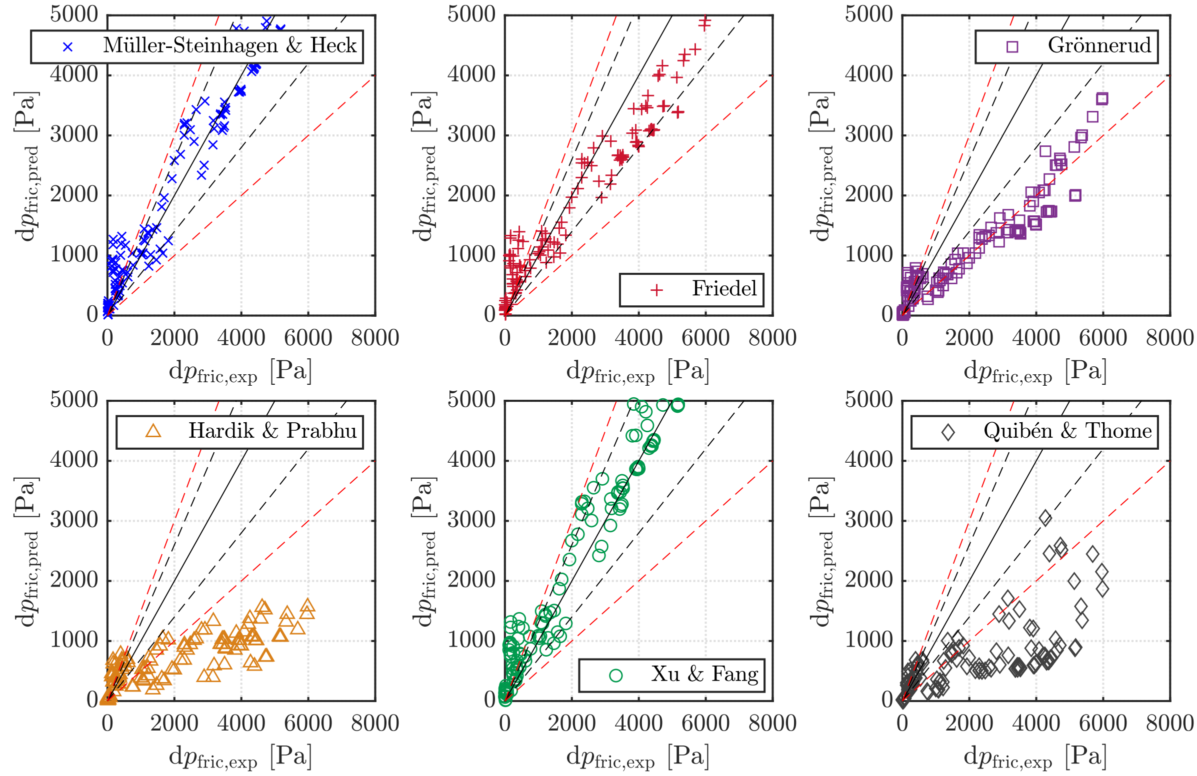

Figure 9: Comparison of predicted and experimental frictional pressure drops using a selection of predictive methods. The solid lines represent $\mathrm{d}p_{\mathrm{pred}} = \mathrm{d}p_{\mathrm{exp}}$, the black dashed lines $\mathrm{d}p_{\mathrm{pred}} = \mathrm{d}p_{\mathrm{exp}} \pm 30\%$, and the red dashed lines $\mathrm{d}p_{\mathrm{pred}} = \mathrm{d}p_{\mathrm{exp}} \pm 50\%$.

experimental data in plots of predicted vs. experimental frictional pressure drop in Fig. 9. Inspection of this figure reveals that the predictions of a subset of these correlations are within ±30% of the experimental data for $\mathrm{d}p_{\mathrm{fric}} > 2000$ Pa. The discrepancies between the predicted and measured pressure drops, however, deteriorate significantly at lower $\mathrm{d}p_{\mathrm{fric}}$ values. This is illustrated further in Fig. 10 which shows a semi-log plot of the ratio of predicted to experimental $\mathrm{d}p_{\mathrm{fric}}$ as a function of vapour quality.

The logarithmic scale used for x in Fig. 10 demonstrates clearly the discrepancy over a vapour quality range, approximately $x = 0.01$-0.05, in which none of the predictive methods perform well. This also corresponds approximately to $\mathrm{d}p_{\mathrm{fric,exp}} > 600\,\mathrm{Pa}$. Particularly towards the lower end of this x-range, the uncertainty in experimental x (0.0085 as shown in Table 2) becomes large compared to its absolute value. More interestingly though, the data points with the largest deviations compared to predictive methods correspond to stratified and slug-type flow patterns. The best-performing predictive method in this x-range is that of Quibén and Thome [29] which, unlike the other methods, is flow-pattern based. This suggests that a phenomenological approach is required for accurate predic-

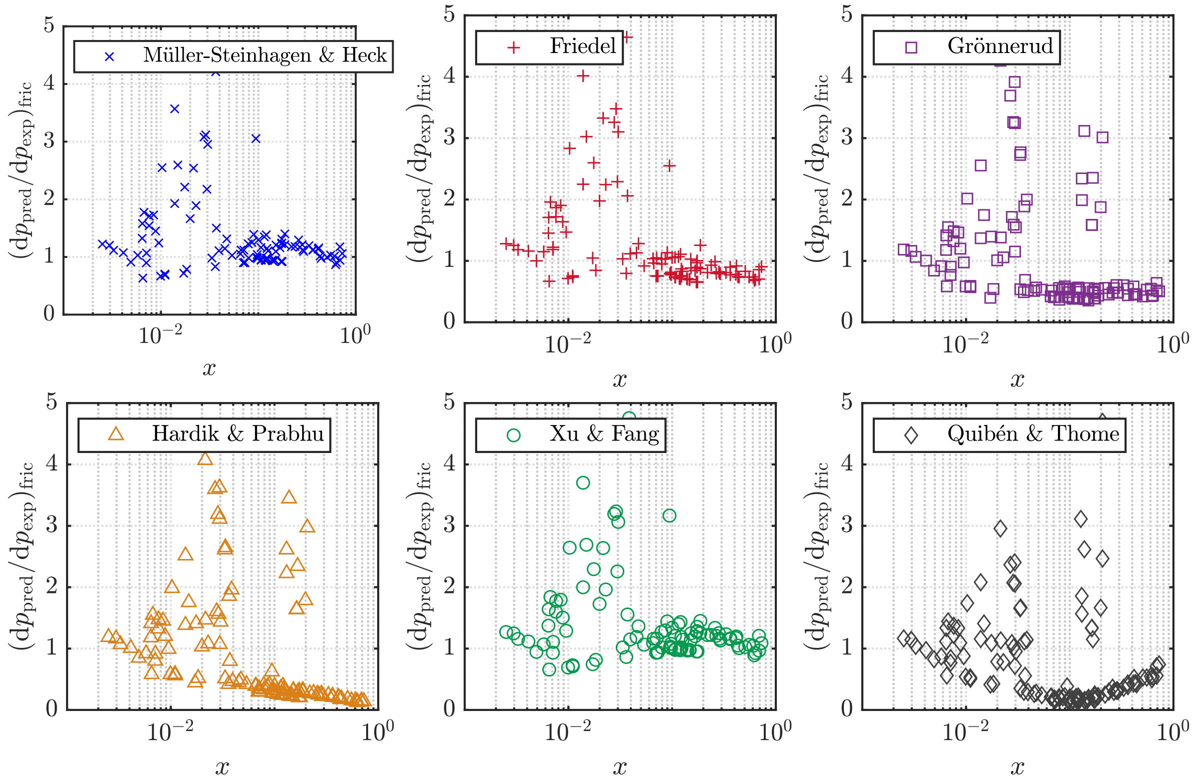

Figure 10: Comparison of predicted and experimental frictional pressure drops using a selection of predictive methods, presented as the ratio of predicted to experimental frictional pressure drop as a function of vapour quality.

Table 3: Summary of the discrepancies between the predicted and experimental pressure drops in terms of the the mean relative deviation (MRD) and mean absolute relative deviation (MARD).

Correlation	MRD (all data) [%]	MARD (all data) [%]	MRD ($\mathrm{d}p_{\mathrm{fric,exp}}$ > 600 Pa) [%]	MARD ($\mathrm{d}p_{\mathrm{fric,exp}}$ > 600 Pa) [%]
Müller-Steinhagen and Heck [25]	+126	481	+6	15
Friedel [20]	+179	563	−13	20
Grönnerud [17]	+3	156	−50	51
Hardik and Prabhu [24]	−9	177	−67	68
Xu and Fang [23]	+134	500	+10	16
Quibén and Thome [29]	−27	130	−69	69

tions of pressure drop in stratified and slug flow patterns at low vapour quality. The prediction accuracy in these regimes could also be improved using detailed measurements of the interface location and velocity fields.

To summarise the performance of the different predictive methods, the mean relative deviation (MRD) and mean absolute relative deviation (MARD) of each, as compared to the experimental data, are presented in Table 3. Values are reported for the full data-set and for the subset $\mathrm{d}p_{\mathrm{fric,exp}} > 600\,\mathrm{Pa}$, which effectively removes the data points with a large uncertainty in x, allowing for a more effective assessment of the applicability of predictive methods to the rest of the data.

Comparing the values reported in Table 3 with inspection of the plots in Fig. 9, the empirical Müller-Steinhagen and Heck [25] correlation most accurately predicts the pressure drop outside of the low-x, low-$\mathrm{d}p_{\mathrm{fric,exp}}$ region. Other authors have found this to be the case over a range of fluids and experimental conditions [18, 22, 23, 26], although they also report deviations of up to 20 % [22]. The Xu and Fang [23] correlation performs similarly well, as Garcia Pabon et al. [67] also found to be true for boiling of R1234yf in 3.2–8.0 mm tubes. This correlation outperforms the other separated flow models of Grönnerud [17] and Friedel [20]. The Grönnerud [17] correlation was developed specifically for refrigerants, but Turgut et al. [18] found it to give accurate results for only a small subset of these fluids. For the experimental data presented here, it underpredicts the pressure drop by approximately 50 %. Whalley [21] compared the Friedel [20] correlation to over 25 000 data points and found it to give the best predictions for most fluids, whilst Xu et al. [22] grouped it amongst the best with Müller-Steinhagen and Heck [25], reporting deviations of up to 30 %, in agreement with the deviation reported in Table 3. Hardik and Prabhu [24] found literature correlations generally underpredicted the pressure drop in comparison to their experimental data for flow boiling of water in 5.5–12 mm tubes, but their resulting correlation does not perform well here for R245fa.

As expected, correlations developed for similar fluids or validated across a wide range of fluids tend to perform better in predicting experimental data. Despite performing well at low vapour qualities, the flow-pattern-based Quibén and Thome [29] correlation underpredicts larger pressure drops. These larger pressure drops mostly correspond to intermittent and annular flow patterns, suggesting that either the flow pattern classification or the corresponding pressure drop predictive method is not in fact suitable for these conditions. The correlation uses the flow pattern classification method of Wojtan et al. [11], which Fig. 6 shows to correctly classify most intermittent and annular data points. In the Quibén and Thome [29] method, the calculated pressure drop for annular flow depends heavily on the interfacial friction factor which was developed based on an experimental data set which did not include R245fa. The prediction of this interfacial friction factor could be enhanced by measuring the velocity field close to the interface using e.g. PIV to understand the shear stresses in this region.

Figure 10 provides an insight into the performance of each predictive method with x. At $x > 0.05$, the Müller-Steinhagen and Heck [25] method, along with the separated flow models of Grönnerud [17], Friedel [20], Xu and Fang [23], performs most consistently with little deviation in the average value of $(\mathrm{d}p_{\mathrm{pred}}/\mathrm{d}p_{\mathrm{exp}})_{\mathrm{fric}}$ as x increases. However, the accuracy of the Hardik and Prabhu [24] method deteriorates as x increases whilst that of the Quibén and Thome [29] method improves. Even though there are relatively few data points in the region $x < 0.05$, the prediction accuracy for all six methods presented in Fig. 10 is almost identical. When x is very small, predictive methods generally collapse to a liquid-only pressure drop, suggesting that at such low vapour qualities the vapour phase does not have a significant impact on $\mathrm{d}p_{\mathrm{fric}}$.

3.3 Comparisons with heat transfer coefficient predictions

Experimental outside wall temperatures were measured at the temperature measurement junctions shown in Fig. 2 for 142 experimental conditions with the parameter ranges G = 30-700 kg/m^2.s, $\dot{q}$ = 0.5–38 kW/m^2. The fluid always entered the measurement section as a subcooled liquid, and the vapour quality was calculated using Eqs. (4) and (5) at each junction according to the corresponding heated length. At the most upstream junction, the fluid is still in the liquid phase and $x = 0$, so measurements from this junction are not included in this section. The reported results are spatially-averaged around the circumference of the pipe by taking the mean of the four wall temperature readings at each junction, and time-averaged over the sampling time.

3.3.1 Flow boiling correlations

Similarly to pressure drops, many predictive methods are available in the literature for estimation of heat transfer coefficients in boiling flows but there is little validation of these methods for R245fa in macroscale tubes. A selection of these methods is presented in terms of predicted vs. experimental h in Fig. 11. Further insight into correlation performance as a function of x is provided by plots of $h_{\text{pred}}/h_{\text{exp}}$ vs. x in Fig. 12, and the mean relative deviations of each method compared to experimental data are detailed in Table 4.

The spread of the data points on the plots in Figs. 11 and 12 varies between methods. Prediction accuracy deviates significantly for several of the selected methods at approximately $h < 1000$ W/m^2.K and $x < 0.05$, with both underprediction and overprediction of h. For these lower values of these parameters the relative uncertainty is larger and can be amplified further by the calculation method. However, some of the methods perform consistently well at this lower end of the parameter ranges, with divergence at higher values. This is most noticeable for the Guo et al. [43] correlation, which is the second-best performing correlation for $x < 0.05$, but the worst for $x > 0.05$. It is also the only method for which $h_{\text{pred}}/h_{\text{exp}}$ increases with x at $x > 0.05$. The correlation was developed based on flow boiling experiments with R245fa and an R134a/R245fa mixture in 3 mm horizontal tubes, and this difference in scale may account for the observed behaviour. At the larger scale of the tube in this work, gravitational effects become more significant with the most relevant effect being the asymmetry of the liquid film between the top and bottom of the tube for flow patterns in which the wall is completely wetted, i.e. slug and annular flows. Most of the data points with larger h or x correspond to slug, annular or intermittent flow. This highlights the importance of using predictive methods developed for similar scales.

The Guo et al. [43] correlation is a modified version of the Liu and Winterton [39] correlation and performs better overall due to the poor predictive capability of the latter at $x < 0.05$. Also, the extent of the underprediction of the Liu and Winterton [39] correlation for $x > 0.05$ increases as $x \to 1$. The Liu and Winterton [39] correlation was developed for tubes with $d > 3$ mm.

The most consistent correlation, and most accurate overall with MARD = 23 %, across the data set, is that of Shah [30] which despite being one of the earliest enhancement-factor correlations has been reported to give reasonable predictions for both boiling [32] and condensation [33] of R245fa in smaller tubes. The Kandlikar [34] correlation is a further development of that Shah [30] and performs similarly well (MARD = 28 %) overall despite larger deviations at $x < 0.05$. Kandlikar [34] introduced a fluid-specific parameter, F_{fl}, to the calculation method and since no such parameter is reported for R245fa it was tuned to the experimental data to a value of $F_{\mathrm{fl}} = 1.3$. The tuning required a trade-off between prediction accuracy low and high values of x and h, so better accuracy could be achieved by using different values for the two regions. The resulting value of $F_{\mathrm{fl}} = 1.3$ is the same as those of R11 and R113 as defined by Kandlikar [34]. These have different chemical structures to R245fa being chloro-fluoro-hydrocarbons of lower carbon number, but R11 particularly has a similar molar mass and boiling point to R245fa. Fang et al. [68] reported a similar accuracy of MARD = 30 % for the Kandlikar [34] correlation applied to R245fa boiling.

After the Shah [30] correlation the flow-pattern based correlation of Wojtan et al. [69] is the next most consistent across the data range despite also tending to underpredict h. This suggests that a flow-pattern based approach is effective for predicting heat transfer despite this not being the case for pressure drop for the full range of x (see Quibén and Thome [29], Fig. 10).

It is clear from the assessment of these predictive methods that a single correlation is rarely effective for the whole data set, and that the applicability of any given correlation is generally restricted to the conditions of the experiment upon which it is based. In their review paper, Thome et al. [70] also found that no single method predicted their entire database well, highlighting the difficulty of finding a universal approach. Many correlations are not well-validated for the low vapour quality region due to high relative uncertainties in integral measurements at the necessary experimental conditions, so detailed spatially and temporally resolved measurements of these flow could provide much-needed insight into the associated flow structures and phenomena.

3.3.2 Pool boiling correlations

One of many ways to predict the dominant boiling mechanism in boiling flow is by evaluation of the convection number, $\mathrm{Cv} = \left(\frac{1-x}{x}\right)^{0.8}\left(\frac{\rho_{\mathrm{v}}}{\rho_{\mathrm{l}}}\right)^{0.5}$, with $\mathrm{Cv} < 0.65$ defining the nucleate boiling dominant zone [34]. Vapour quality is perturbed the most, up to two orders of magnitude, of all experimental parameters investigated in this study, whilst other parameters affecting the establishment of nucleate boiling-dominated conditions, such as mass velocity and surface roughness, do not change as much, if at all, over the data set.

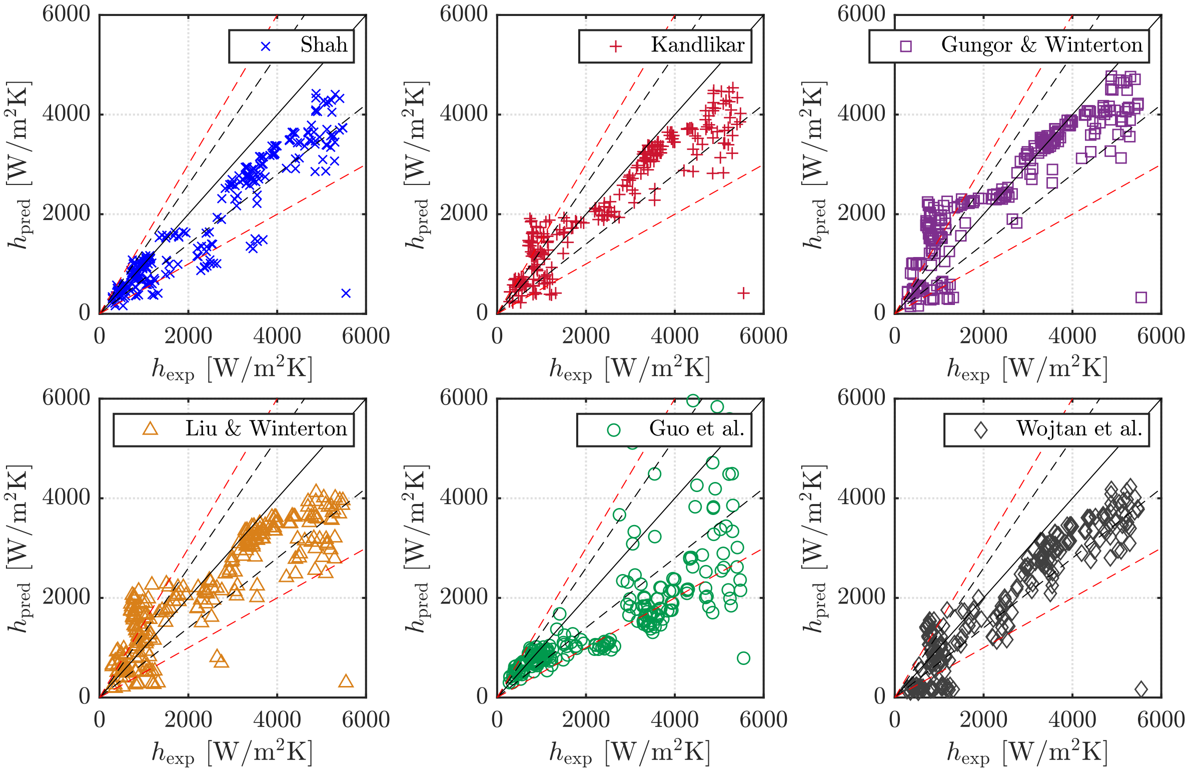

Figure 11: Comparison of predicted and experimental frictional heat transfer coefficients using a selection of predictive methods. The solid lines represent $h_{\text{pred}} = h_{\text{exp}}$, the black dashed lines $h_{\text{pred}} = h_{\text{exp}} \pm 30\%$, and the red dashed lines $h_{\text{pred}} = h_{\text{exp}} \pm 50\%$.

Table 4: Summary of the discrepancies between the predicted and measured heat transfer coefficients in terms of the mean relative deviation (MRD) and mean absolute relative deviation (MARD).

Correlation	MRD (all data)	MARD (all data)	MARD ($x > 0.05$)	MARD ($x < 0.05$)
Shah [30]	−19	23	23	24
Kandlikar [34]	+3	28	19	41
Gungor and Winterton [38]	+18	37	17	67
Liu and Winterton [39]	+7	37	23	58
Guo et al. [32]	−20	36	41	28
Wojtan et al. [69]	−20	33	31	37

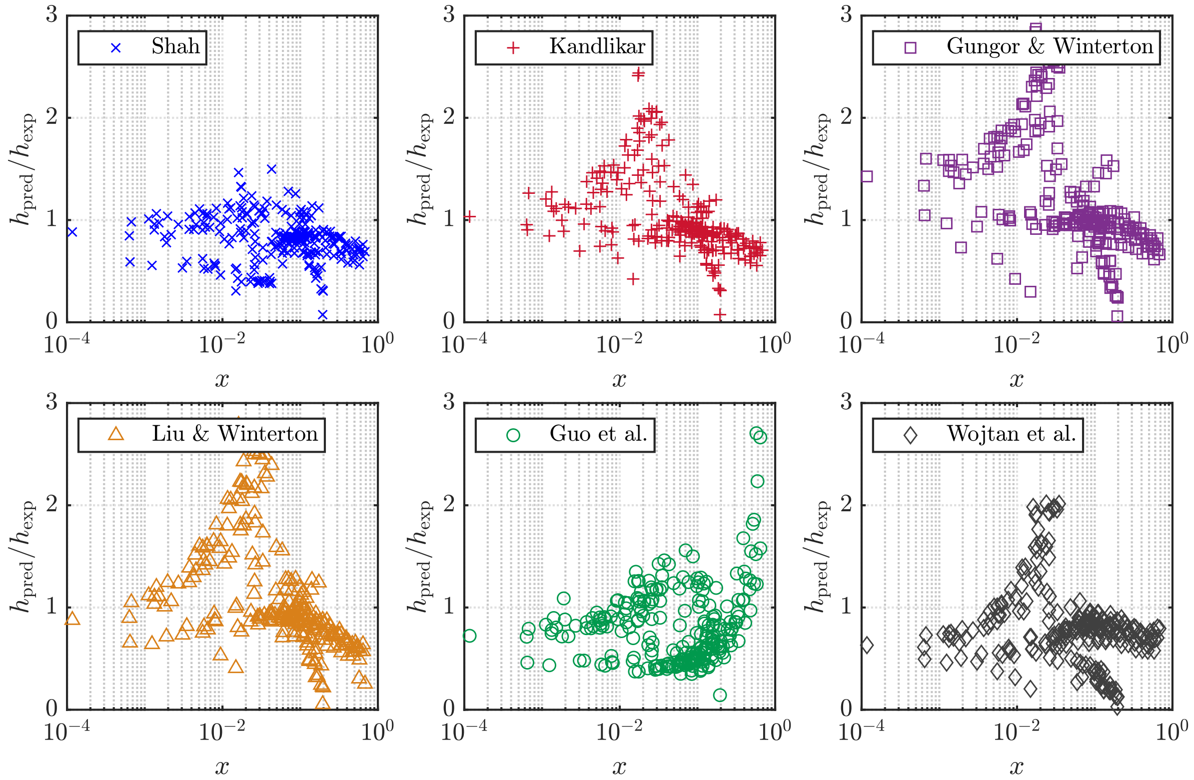

Figure 12: Ratio of predicted to experimental frictional heat transfer coefficients plotted against vapour quality using a selection of predictive methods.

This is reflected in the operation of real engineering systems utilising flow boiling, so Cv was selected as an appropriate characterisation parameter. Considering the experimental heat transfer coefficient data, 46 % of the points fall into the nucleate boiling dominant zone as defined by the condition Cv < 0.65. The heat transfer behaviour in this zone could be described by pool boiling correlations. These are not a function of vapour quality or mass flux, so should not be affected by the large proportional uncertainties discussed for flow boiling correlations, but are simply dependent on the fluid and pipe properties, and on empirical constants.

Six pool boiling correlations were selected and the ratios of the resulting heat transfer coefficient to the corresponding experimental h are plotted as a function of the measured h values in Fig. 13. The corresponding deviations are given in Table 5.

With the exception of the Mostinski [71] correlation, the reduced pressure-based correlations (Cooper [72], Gorenflo [73], Ribatski and Jabardo [74]) provide the most accurate predictions of the experimental data. Chen [31] also found the Cooper [72] correlation to give reasonable predictions for h for pool boiling of R245fa on a cylinder. The performance of the Gorenflo [73] correlation depends on the reference h, for which a tabulated value for R245fa is not provided. The appropriate value was thus determined by fitting of the experimental data, but interestingly this still does not provide the best fit according to Table 5. The Gorenflo and Kenning [75] correlation provided a modified and improved version of the Gorenflo [73] correlation, but included several fluid specific correction factors as well as reference values which are not yet provided for R245fa. A more accurate prediction could be obtained by further investigation of the correct values of these factors for R245fa.

Based on Table 5, the Ribatski and Jabardo [74] correlation is most accurate, and Fig. 13 shows that it underpredicts h at high values of h_{exp} to a lesser extent than most of the other correlations. The empirical constants in the Ribatski and Jabardo [74] correlation are pipe-specific rather than fluid-specific and are well-defined for stainless steel, unlike the fluid-specific quantities for R245fa.

The Stephan and Abdelsalam [76] correlation underpredicts h significantly, despite claiming to be valid for the experimental conditions. This thermo-physical property-based correlation is a function of the bubble departure diameter, calculated based on the contact angle β which the authors advise to assign the value of $35°$ for all refrigerants. Halon et al. [77] found this correlation to give a poor prediction of h for pool boiling of R245fa on a heated plate, finding deviations of up to 157 % and suggesting that it overestimates the effects of $\dot{q}$ and T_{sat} on h. The empirical correlation of Jung et al. [78] uses the same calculation of bubble departure diameter, but the term containing this value, $\dot{q}$ and T_{sat} is raised to a different value to that in the Stephan and Abdelsalam [76] equation. In the Jung et al. [78] equation this value is calculated based on fluid properties, the reduced pressure and empirical constants. These empirical constants could be better tuned for these experiments to improve the prediction accuracy.

Overall, the experimental heat transfer coefficient is not well-predicted by pool boiling correlations, particularly at low values of h_{exp}. This suggests that convective heat transfer cannot be neglected at these conditions and superposition approaches, such as that of Liu et al. [33] as investigated in Figs. 11 and 12 are more appropriate. This contribution of convective boiling effects is to be expected at the low heat fluxes associated with the low h_{exp} data points, and due to R245fa being a low pressure refrigerant with a correspondingly high vapour specific volume that results in high two-phase flow velocities.

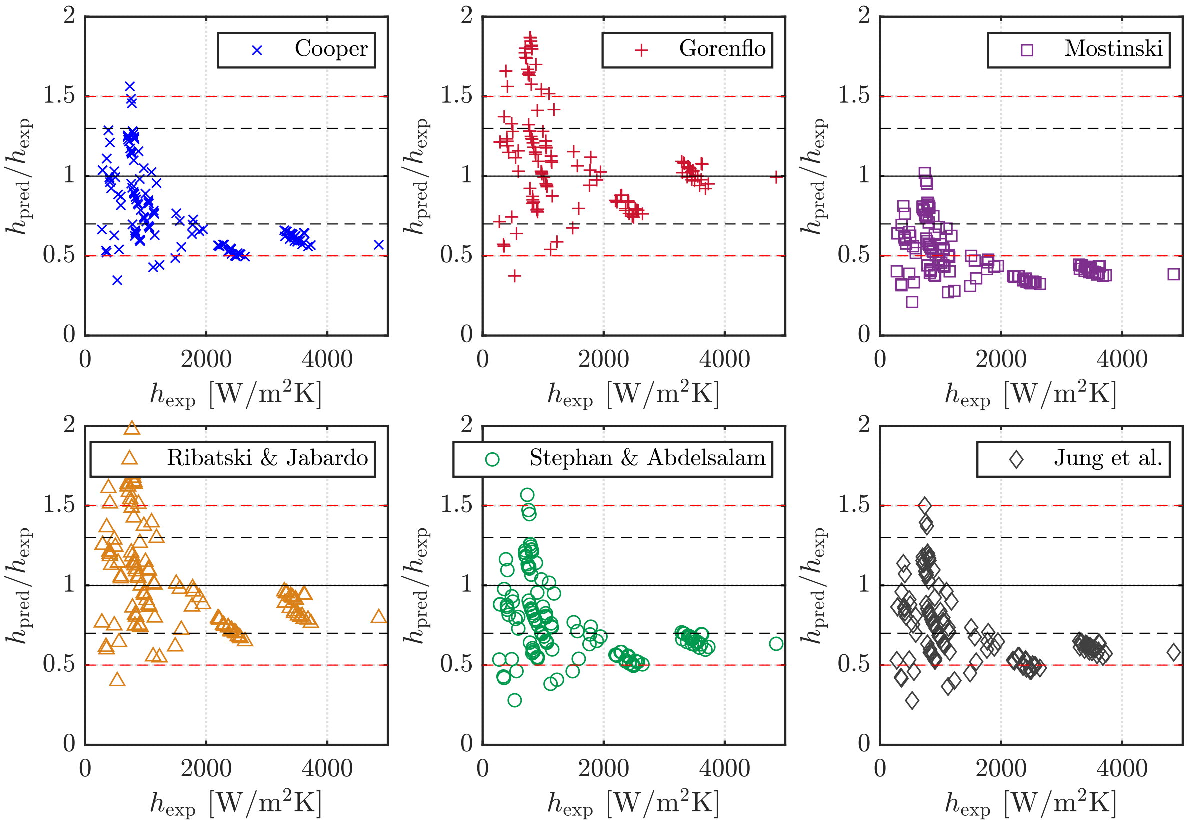

Figure 13: Ratio of predicted to experimental frictional heat transfer coefficients plotted against experimental heat transfer coefficient for data in the nucleate boiling dominant zone.

Table 5: Summary of discrepancies between the predicted and measured pool boiling heat transfer coefficients in terms of mean relative deviation (MRD) and mean average relative deviation (MARD).

Correlation	MRD	MARD
Cooper [72]	−21	30
Gorenflo [73]	+12.7	27
Mostinski [71]	−49	49
Ribatski and Jabardo [74]	+3	26
Stephan and Abdelsalam [76]	−24	31
Jung et al. [78]	−27	32

3.4 Detailed laser-based measurements

In this section, results obtained by applying the laser-based measurement methods described in Section 2.1.2 are presented and discussed. Boiling in the flows investigated in this work has not been previously investigated with such laser-based methods, which enable us to obtain detailed spatiotemporally resolved information, and to link this information to the integral thermohydraulic data on flow regimes, pressure drops and heat transfer presented in previous sections.

Figure 14 shows an instantaneous velocity field in a stratified-wavy flow with the parameters $G = 73$ kg/m^2.s, $\dot{q} = 2.6\,\mathrm{kW/m^2}$. The vapour-liquid interface is marked with a black line, and has an uncertainty of $\pm$ 0.16 mm. It can be seen from the changes in direction of the arrows that the wave induces secondary flows, particularly at the crest where the flow accelerates in both the streamwise and vertical directions. These secondary flows, particularly as waves become larger, can move liquid away from the heated wall as they disturb the layer of unidirectional streamwise flow close to the wall. This effect can be observed in Fig. 14, particularly towards the right-hand side ahead of the wave crest where the velocity vector arrows closest to the wall show the presence of a non-zero y-component of the velocity. As a result of this, hot fluid close to the heated tube wall is moved away and replaced with cooler fluid. This increases the temperature gradient between the wall and the liquid and therefore increases increases the rate of heat transfer.

For the stratified-wavy flow shown in Fig. 14 the average heat transfer coefficient at the furthest downstream measurement junction (see Fig. 2) is 26 % larger than that for a stratified flow of equal heat flux and 45 % larger mass flux. Since h generally decreases with decreasing mass flux in convective boiling [24, 32], this contradictory increase in h for the stratified-wavy flow is likely to be a result of the flow structures as described in the previous paragraph. This effect was found to be consistent across all investigated conditions with a comparable heat flux, suggesting a pronounced heat transfer enhancement due to interfacial waviness. The interface location data obtained using the image processing techniques described in Section 2.1.2 can be used to quantitatively characterise the interface by performing statistical analysis of the waves. The resulting quantities could be compared to integral pressure drop and heat transfer measurements to determine the impact of wave characteristics on these values. Phase lock averaging techniques, such as those employed by Charogiannis et al. [55] could then be used to understand the be-

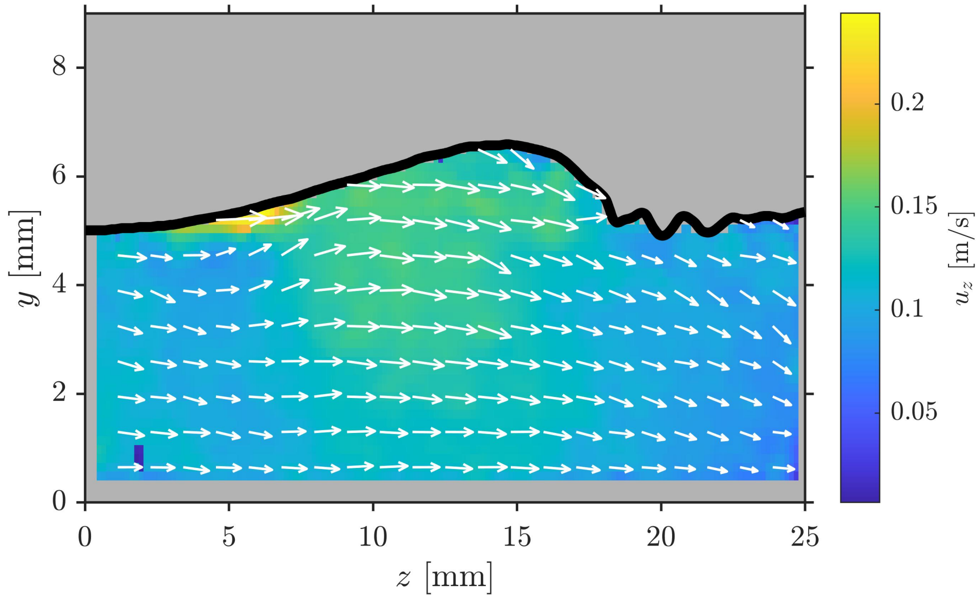

Figure 14: Instantaneous liquid-phase velocity field in a stratified wavy flow, $G = 73$ kg/m^2.s, $\dot{q} = 2.6\,\mathrm{kW/m^2}$, $x = 0.13$, $d = 12.6\,\mathrm{mm}$. The interface is identified with the black line and the length of the arrows represents the magnitude of the velocity vector, whilst the colour map in the background represents the magnitude of the velocity in the streamwise direction, z.

haviour of the velocity field around wave peaks and troughs. Further analysis of these phenomenon using such approaches is required and will be addressed in future studies. Also, the detailed information on interface location and velocity could be used to improve flow patterns maps and flow-pattern based predictive methods for pressure drop [29] and heat transfer [69].

In stratified flows, the secondary flows seen in Fig. 14 are not present, so instantaneous velocity fields follow a typical Poiseuille flow structure. Interesting information is instead obtained by averaging the velocity field temporally and spatially along the streamwise direction to obtain an average velocity field in that direction as a function of the vertical direction, y. Fig. 15 shows four such velocity fields obtained at $\dot{q} = 1.7\,\mathrm{kW/m^2}$ for different values of G, with y scaled by the corresponding interface height y_{int} for each case. The corresponding interface heights and other relevant data can be found in Table 6. On visual inspection, the velocity profiles behave as expected for the denser phase of a stratified flow [79], with the velocity going to 0 towards the wall ($y = 0$) and reaching its maximum value close to the interface ($y/y_{\mathrm{int}} = 1$). At the lowest mass flux ($G = 32$ kg/m^2.s) the velocity increases steadily as the distance from the wall increases before reaching a maximum near the interface, as expected for laminar stratified flows [80]. The liquid-only Reynolds number at the heated pipe inlet for this condition is Re $= 1070$, so the flow enters the test section in the laminar regime. As Re increases into the transitional and eventually turbulent regimes, the profile flattens and $u_{z,\max}$ increases in magnitude and is reached away from the interface. Further investigation is required into any impact of heat transfer on these profiles when compared to those in stratified gas-liquid flows without phase change.

The average experimental heat transfer coefficient at the furthest downstream measurement junction (see Fig. 2) for each case in Fig. 15 is reported in Table 6. In boiling flows, generally h increases with increasing G, although this effect has been observed to become more prominent with increasing vapour quality such that at very low x, G has little impact on h [43, 46, 81]. However, Lillo et al. [82] observed the opposite effect at $x < 0.2$ with h decreasing with increasing G. This effect is also exhibited by the values in Table 6, where the highest value of h_{exp} corresponds to the lowest value of G and vice versa. It is also evident that h_{exp} increases with decreasing interface height, and h_{exp} is considerably higher when the vapour liquid interface height is below the centreline ($y = 6.3\,\mathrm{mm}$). In stratified flow, the heat transfer is dominated by the liquid phase travelling along the bottom of the pipe, which has a larger heat capacity than the vapour phase. When the film is thin, there is lower resistance to heat transfer and for the conditions presented here this film effect is greater than the effect of increased turbulence due to increasing G. Markides et al. [83] observed similar heat transfer enhancement in thin-film regions using PLIF and IR to investigate falling film flows over an inclined heated foil.

The flow-pattern based Wojtan et al. [69] predictive method for h is based on the prediction of the stratified angle, θ_{strat} (see Eq. (11)), and the liquid film thickness. However, the method tends to underpredict h, as shown in Fig. 12. A larger set of experimental data such as that reported in Table 6 could thus be used to improve the prediction of θ_{strat} and thus h in stratified flows. This would also aid the identification of the stratified region on flow pattern maps, allowing accurate predictions of the conditions at which stratified flow occurs. Since stratified flow is less effective for heat transfer than flow regimes such as annular in which the whole perimeter is wetted, it is desirable to avoid it in heat transfer applications and accurately predicting its onset is vital.

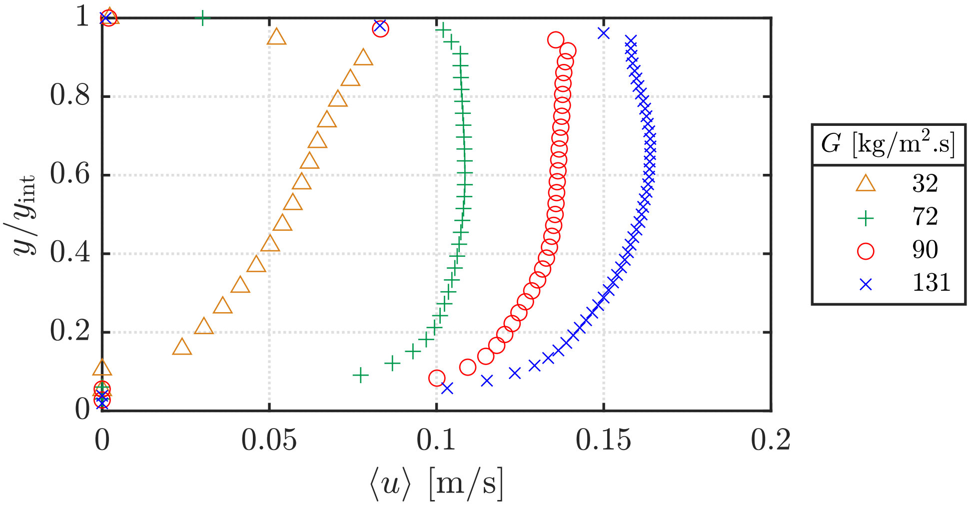

Figure 15: Streamwise velocity profiles, averaged over the streamwise direction and time, for stratified flow with $\dot{q} = 1.7\,\text{kW/m}^2$ at a range of mass fluxes, with the vertical direction y scaled by the corresponding interface height y_{int} for each case.

Table 6: Stratified flow experimental parameters and results for $\dot{q} = 1.7\,\text{kW/m}^2$

G [kg/m^2.s]	x [-]	$u_{z,\text{max}}$ [m/s]	y_{int} [mm]	h_{exp} [kW/m^2.K]
32	0.210	0.08	3.6	1.2
72	0.082	0.11	6.6	0.43
90	0.063	0.13	6.8	0.43
150	0.018	0.16	9.0	0.36

3.5 Implications for flow boiling applications

The results presented in this work have direct implications for the design and operation of flow boiling systems such as concentrating solar power plants, refrigeration and heat pumps systems, and waste heat recovery and conversion systems. Identifying the most accurate predictive methods for flow pattern, pressure drop and heat transfer allows design engineers to select the most appropriate correlations for their system and optimise the design parameters accordingly. In ORC systems heat exchangers dominate the total investment cost [84, 85], with the evaporator alone accounting for at least a third of the total cost in systems with an n-alkane-type working fluid such as R245fa [86, 87]. Since the cost of a heat exchanger is directly related to the heat transfer area, accurate prediction of heat transfer performance is vital. The heat transfer area will also affect the footprint of the heat exchanger, which has further cost implications in terms of equipment size and space.

In concentrating solar power systems operating under the direct steam generation mode it is important to know the flow pattern under which the flow in the long solar receiver tubes is operating. Stratified flow in these tubes can result in large circumferential temperature gradients [88, 89], which can in turn cause bending of the tubes and severe, and costly, damage to the system. Accurate prediction of the heat transfer in the desired flow regimes, through use of appropriate correlations, is also key to the design of these systems, since under- or over-sizing can result in inefficiencies and associated cost penalties. In industrial applications, flow-pattern specific models can be prohibitively complex to implement, but detailed measurements of these boiling flows could enable identification of areas for improvement and simplification. Although solar receiver tubes in concentrating solar power systems can be subject to non-uniform and transient heat fluxes, the results of this study under uniform, constant heat flux provide useful insights into relevant flow boiling phenomena and can be used as a benchmark for further investigations in this experimental facility with spatially and temporally varying heat flux.

The operational costs of all flow boiling systems are affected by the power requirements of the pump, although the capital cost of the pump is relatively small compared to that of the heat exchangers [86, 87]. It is thus important to understand the most accurate predictive methods for pressure drop of boiling flows, as investigated in this work.

This work, whilst motivated by the aforementioned applications, does not aim to replicate their operating conditions exactly. Instead, its purpose is to provide insight, including detailed measurements, into flow boiling phenomena within the limitations of the experimental facility. The data and results could be directly compared to applications with low pressure operating conditions, whilst some further work is required to investigate how the findings can be applied to, e.g., ORC systems.

4 Conclusions

A bespoke experimental facility has been constructed, commissioned and validated for the characterisation of flow boiling of R245fa in a 12.6 mm inside diameter horizontal pipe. Experimental information has been collected including pressure drops, heat transfer measurements and both qualitative and quantitative flow visualisations.

Since the applicability of predictive methods in the literature to this fluid (R245fa), geometry (d_i =12.6 mm) and experimental conditions is not widely reported, comparisons of experimental results to predictive methods for flow pattern maps, pressure drops and heat transfer coefficients have been made. The nominations of flow patterns put forward by Wojtan et al. [11] were found to describe the range of observed flow patterns well, but it was not possible to observe mist and dryout flows in this experimental facility. However, the Wojtan et al. [11] map did not accurately describe the transitions between slug and stratified flow types, with the Zürcher et al. [14] formulation of this transition line better fitting the experimental data. The intermittent-annular transition lines also require some modification to fit the data set generated in this work.

The experimental frictional pressure drop was most accurately described at high vapour qualities by the Müller-Steinhagen and Heck [25] and Xu and Fang [23] methods, although accurate prediction was not achieved by any of the tested methods at very low vapour qualities. Correlations for heat transfer coefficient were more accurate across the dataset, with the Shah [30] method proving the most consistently accurate, followed by the flow-pattern based model of Wojtan et al. [69]. This suggests that a flow-pattern based approach is appropriate for prediction of heat transfer, despite this not being the case for pressure drop across the full vapour quality range. A significant proportion of experimental data points fell into the nucleate boiling dominant zone, so the applicability of pool boiling correlations was also investigated. Many of these methods rely on empirical constants and fluid specific parameters which require further tuning for R245fa flow at this scale.

Results from the application of laser-based diagnostic techniques specifically developed for these flows were also presented. Planar laser-induced fluorescence was employed to identify the vapour-liquid interface, and particle image velocimetry was used to investigate the velocity fields inside these flows. Secondary flows were observed in the liquid phase of a stratified-wavy flow and linked to enhanced heat transfer as compared to stratified flow at similar conditions. Decreasing vapour-liquid interface height in stratified flow was associated with enhanced heat transfer, despite the corresponding mass flux increasing. These detailed spatiotemporally resolved measurements in boiling flows represent an important contribution to the literature and can provide insights into the interaction of hydrodynamic and heat transfer phenomena in these systems, and improve our understanding of boiling in many important applications, including refrigeration and heat-pump systems, waste-heat recovery and conversion systems and concentrating solar power technology. The data can also be used for advanced multiphase model development and validation.

Acknowledgements

The work was supported by Russian Government "Megagrant" project 075-15-2019-1888, the UK Department for International Development (DFID) through the Royal Society-DFID Africa Capacity Building Initiative, and the UK Engineering and Physical Sciences Research Council (EPSRC) [grant numbers EP/P004709/1 and EP/L020564/1]. Data supporting this publication can be obtained on request from cep-lab@imperial.ac.uk.

References

[1] E. Galloni, G. Fontana, and S. Staccone. Design and experimental analysis of a mini ORC (organic Rankine cycle) power plant based on R245fa working fluid. *Energy*, 90:768–775, 2015. doi: 10.1016/j.energy.2015.07.104.

[2] S.H. Kang. Design and experimental study of ORC (organic Rankine cycle) and radial turbine using R245fa working fluid. *Energy*, 41(1):514–524, 2012. doi: 10.1016/j.energy.2012.02.035.

[3] J. Freeman, I. Guarracino, S.A. Kalogirou, and C. N. Markides. A small-scale solar organic Rankine cycle combined heat and power system with integrated thermal energy storage. *Applied Thermal Engineering*, 127:1543–1554, 2017. doi: 10.1016/j.applthermaleng.2017.07.163.

[4] A. Ramos, M.A. Chatzopoulou, J. Freeman, and C.N. Markides. Optimisation of a high-efficiency solar-driven organic Rankine cycle for applications in the built environment. *Applied Energy*, 228:755–765, 2018. doi: 10.1016/j.apenergy.2018.06.059.

[5] A.M. Pantaleo, M. Simpson, G. Rotolo, E. Distaso, O.A. Oyewunmi, P. Sapin, P. De Palma, and C.N. Markides. Thermoeconomic optimisation of small-scale organic Rankine cycle systems based on screw vs. piston expander maps in waste heat recovery applications. *Energy Conversion and Management*, 200:112053, 2019. doi: 10.1016/j.enconman.2019.112053.

[6] M.A. Chatzopoulou, S. Lecompte, M. De Paepe, and C.N. Markides. Off-design optimisation of organic Rankine cycle (ORC) engines with different heat exchangers and volumetric expanders in waste heat recovery applications. *Applied Energy*, 253: 113442, 2019. doi: 10.1016/j.apenergy.2019.113442.

[7] A. Fernández-García, E. Zarza, L. Valenzuela, and M. Pérez. Parabolic-trough solar collectors and their applications. *Renewable and Sustainable Energy Reviews*, 14(7): 1695–1721, 2010. doi: 10.1016/j.rser.2010.03.012.

[8] S. G. Kandlikar and W. J. Grande. Evolution of microchannel flow passages– thermohydraulic performance and fabrication technology. *Heat Transfer Engineering*, 24 (1):3–17, 2003.

[9] A. Landelle, N. Tauveron, P. Haberschill, R. Revellin, and S. Colasson. Organic Rankine cycle design and performance comparison based on experimental database. *Applied Energy*, 204:1172–1187, 2017. doi: 10.1016/j.apenergy.2017.04.012.

[10] N. Kattan, J.R. Thome, and D. Favrat. Flow boiling in horizontal tubes: Part 1—Development of a diabatic two-phase flow pattern map. *Journal of Heat Transfer*, 120(1):140–147, 1998. doi: 10.1115/1.2830037.

[11] L. Wojtan, T. Ursenbacher, and J.R. Thome. Investigation of flow boiling in horizontal tubes: Part I - A new diabatic two-phase flow pattern map. *International Journal of Heat and Mass Transfer*, 48(14):2955–2969, 2005. doi: 10.1016/j.ijheatmasstransfer.2004.12.012.

[12] C.L. Ong and J.R. Thome. Macro-to-microchannel transition in two-phase flow: Part 1 - Two-phase flow patterns and film thickness measurements. *Experimental Thermal and Fluid Science*, 35(1):37–47, 2011. doi: 10.1016/j.expthermflusci.2010.08.004.

[13] E. Costa-Patry and J.R. Thome. Flow pattern-based flow boiling heat transfer model for microchannels. *International Journal of Refrigeration*, 36(2):414–420, 2013. doi: 10.1016/j.ijrefrig.2012.12.006.

[14] O. Zürcher, J.R. Thome, and D. Favrat. Evaporation of ammonia in a smooth horizontal tube: Heat transfer measurements and predictions. *Journal of Heat Transfer*, 121(1):89–101, 1999. doi: 10.1115/1.2825974.

[15] P.E.L. Barbieri, J.M.S. Jabardo, and E.P.B. Filho. Flow patterns in convective boiling of refrigerant R-134a in smooth tubes of several diameters. In *5th European Thermal-Sciences Conference*, 2008.

[16] R.W. Lockhart and R.C. Martinelli. Proposed correlation of data for isothermal two-phase, two-component flow in pipes. *Chem. Eng. Prog.*, 45(1):39–48, 1949.

[17] R. Grönnerud. Investigation of liquid holdup, flow resistance and heat transfer in circulation type evaporators, part IV: Two-phase resistance in boiling refrigerants. *Bull. I'Inst. Du Froid*, 16(Annexe 1):1972–1981, 1972.

[18] O.E. Turgut, M.T. Çoban, and M. Asker. Comparison of flow boiling pressure drop correlations for smooth macrotubes. *Heat Transfer Engineering*, 37(6):487–506, 2016. doi: 10.1080/01457632.2015.1060733.

[19] B.K. Hardik, G. Kumar, and S.V. Prabhu. Boiling pressure drop, local heat transfer distribution and critical heat flux in horizontal straight tubes. *International Journal of Heat and Mass Transfer*, 113:466–481, 2017. doi: 10.1016/J.IJHEATMASSTRANSFER.2017.05.073.

[20] L. Friedel. Improved friction pressure drop correlations for horizontal and vertical two-phase pipe flow. *Rohre - Rohreleitungsbau - Rohreleitungstransport Int.*, 18:485–491, 1979.

[21] P.B. Whalley. Multiphase Flow and Pressure Drop. In *Heat Exchanger Design Handbook*, pages 2.3.2–11. Hemisphere, Washington, D.C., vol. 2 edition, 1983.

[22] Y. Xu, X.D. Fang, S. Xianghui, Z. Zhou, and W. Chen. Evaluation of frictional pressure drop correlations for two-phase flow in pipes. *Nuclear Engineering and Design*, 253:86–97, 2012. doi: 10.1016/j.nucengdes.2012.08.007.

[23] Y. Xu and X. Fang. A new correlation of two-phase frictional pressure drop for evaporating flow in pipes. *International Journal of Refrigeration*, 35(7):2039–2050, 2012. doi: 10.1016/j.ijrefrig.2012.06.011.

[24] B.K. Hardik and S.V. Prabhu. Boiling pressure drop and local heat transfer distribution of water in horizontal straight tubes at low pressure. *International Journal of Thermal Sciences*, 110:65–82, 2016. doi: 10.1016/j.ijthermalsci.2016.06.025.

[25] H. Müller-Steinhagen and K. Heck. A simple friction pressure drop correlation for two-phase flow in pipes. *Chemical Engineering and Processing: Process Intensification*, 20(6):297–308, 1986. doi: 10.1016/0255-2701(86)80008-3.

[26] C. Tribbe and H.M. Müller-Steinhagen. An evaluation of the performance of phenomenological models for predicting pressure gradient during gas-liquid flow in horizontal pipelines. *International Journal of Multiphase Flow*, 26(6):1019–1036, 2000. doi: 10.1016/S0301-9322(99)00070-1.

[27] D. Mikielewicz. A new method for determination of flow boiling heat transfer coefficient in conventional-diameter channels and minichannels. *Heat Transfer Engineering*, 31(4):276–287, 2010. doi: 10.1080/01457630903311694.

[28] D. Mikielewicz, J. Wajs, R. Andrzejczyk, and M. Klugmann. Pressure drop of HFE7000 and HFE7100 during flow condensation in minichannels. *International Journal of Refrigeration*, 68:226–241, 2016. doi: 10.1016/j.ijrefrig.2016.03.005.

[29] J. Quibén and J.R. Thome. Flow pattern based two-phase frictional pressure drop model for horizontal tubes. Part I: Diabatic and adiabatic experimental

study. *International Journal of Heat and Fluid Flow*, 28:1049–1059, 2007. doi: 10.1016/j.ijheatfluidflow.2007.01.003.

[30] M.M. Shah. Chart correlation for saturation boiling heat transfer: Equation and further study. *ASHREA Transactions*, 88(1):185–196, 1982.

[31] J.C. Chen. Correlation for boiling heat transfer to saturated fluids in convective flow. *Industrial & Engineering Chemistry Process Design and Development*, 5(3):322–329, 1966. doi: 10.1021/i260019a023.

[32] Q. Guo, M. Li, and X. Tian. Experimental study on flow boiling heat transfer characteristics of R134a, R245fa and R134a/R245fa mixture at high saturation temperatures. *International Journal of Thermal Sciences*, 150:106195, 2020. doi: 10.1016/j.ijthermalsci.2019.106195.

[33] S. Liu, M. Song, B. Dai, Y. Tian, M. Song, and N. Mao. Experimental study on R245fa condensation heat transfer in horizontal smooth tube and enhanced tube. In *Energy Procedia*, volume 142, pages 4169–4175. Elsevier Ltd, 2017. doi: 10.1016/j.egypro.2017.12.342.

[34] S.G. Kandlikar. A general correlation for saturated two-phase flow boiling heat transfer inside horizontal and vertical tubes. *Journal of Heat Transfer*, 112(1):219–228, 1990. doi: 10.1115/1.2910348.

[35] J.M. Saiz Jabardo, E.P. Bandarra Filho, and C.U. Da Silva Lima. New correlation for convective boiling of pure halocarbon refrigerants flowing in horizontal tubes. *Revista Brasileira de Ciencias Mecanicas/Journal of the Brazilian Society of Mechanical Sciences*, 21(2):245–258, 1999.

[36] A. Greco and G. P. Vanoli. Flow boiling heat transfer with HFC mixtures in a smooth horizontal tube. Part II: Assessment of predictive methods. *Experimental Thermal and Fluid Science*, 29(2):199–208, 2005. doi: 10.1016/j.expthermflusci.2004.03.004.

[37] J. Yong Kim and A.J. Ghajar. A general heat transfer correlation for non-boiling gas-liquid flow with different flow patterns in horizontal pipes. *International Journal of Multiphase Flow*, 32(4):447–465, 2006. doi: 10.1016/j.ijmultiphaseflow.2006.01.002.

[38] K.E. Gungor and R.H.S. Winterton. A general correlation for flow boiling in tubes and annuli. *International Journal of Heat and Mass Transfer*, 29(3):351–358, 1986. doi: 10.1016/0017-9310(86)90205-X.

[39] Z. Liu and R.H.S. Winterton. A general correlation for saturated and subcooled flow boiling in tubes and annuli, based on a nucleate pool boiling equation. *International Journal of Heat and Mass Transfer*, 34(11):2759–2766, 1991. doi: 10.1016/0017-9310(91)90234-6.

[40] D. Steiner and J. Taborek. Flow boiling heat transfer in vertical tubes correlated by an asymptotic model. *Heat Transfer Engineering*, 13(2):43–69, 1992. doi: 10.1080/01457639208939774.

[41] J.P. Wattelet, J.C. Chato, B.R. Christoffersen, J.A. Gaibel, M. Ponchner, P.J. Kenney, R.L. Shimon, T.C. Villaneuva, N.L. Rhines, K.A. Sweeney, D.G. Allen, and T.T. Hershberger. Heat transfer flow regimes of refrigerants in a horizontal-tube evaporator. Technical report, Air Conditioning and Refrigeration Center, Univeristy of Illinois, Urbana, IL, 1994.

[42] S. Yuan, W.L. Cheng, Y.L. Nian, Q. Zhong, Y.F. Fan, and J. He. Evaluation of prediction methods for heat transfer coefficient of annular flow and a novel correlation. *Applied Thermal Engineering*, 114:10–23, 2017. doi: 10.1016/j.applthermaleng.2016.11.170.

[43] C. Guo, J. Wang, X. Du, and L. Yang. Experimental flow boiling characteristics of R134a/R245fa mixture inside smooth horizontal tube. *Applied Thermal Engineering*, 103:901–908, 2016. doi: 10.1016/j.applthermaleng.2016.04.162.

[44] N. Kattan, J.R. Thome, and D. Favrat. Flow boiling in horizontal tubes: Part 3—Development of a new heat transfer model based on flow pattern. *Journal of Heat Transfer*, 120(1):156–165, 1998. doi: 10.1115/1.2830039.

[45] D. Mikielewicz and J. Mikielewicz. A common method for calculation of flow boiling and flow condensation heat transfer coefficients in minichannels with account of nonadiabatic effects. *Heat Transfer Engineering*, 32(13-14):1173–1181, 2011. ISSN 0145-7632. doi: 10.1080/01457632.2011.562728.

[46] S. Grauso, R. Mastrullo, A.W. Mauro, J.R. Thome, and G.P. Vanoli. Flow pattern map, heat transfer and pressure drops during evaporation of R-1234ze(E) and R134a in a horizontal, circular smooth tube: Experiments and assessment of predictive methods. *International Journal of Refrigeration*, 36(2):478–491, 2013. doi: 10.1016/J.IJREFRIG.2012.07.016.

[47] D. Wang, L. Zhao, X. Nie, Y. Lu, and S. Deng. Experimental study on flow boiling characteristics of R-245fa in circular tube under non-uniform heat flux. *International Journal of Heat and Mass Transfer*, 143:118570, 2019. doi: 10.1016/j.ijheatmasstransfer.2019.118570.

[48] T. Ursenbacher, L. Wojtan, and J.R. Thome. Interfacial measurements in stratified types of flow. Part I: New optical measurement technique and dry angle measurements. *International Journal of Multiphase Flow*, 30(2):107–124, 2004. doi: 10.1016/j.ijmultiphaseflow.2003.11.010.

[49] C.E. Estrada-Perez and Y.A. Hassan. PTV experiments of subcooled boiling flow through a vertical rectangular channel. *International Journal of Multiphase Flow*, 36 (9):691–706, 2010. doi: 10.1016/J.IJMULTIPHASEFLOW.2010.05.005.

[50] Y.A. Hassan, C.E. Estrada-Perez, and Jun Soo Yoo. Measurement of subcooled flow boiling using Particle Tracking Velocimetry and infrared thermographic technique. *Nuclear Engineering and Design*, 268:185–190, 2014. doi: 10.1016/J.NUCENGDES.2013.04.044.

[51] R. Samaroo, N. Kaur, K. Itoh, T. Lee, S. Banerjee, and M. Kawaji. Turbulent flow characteristics in an annulus under air bubble injection and subcooled flow boiling conditions. *Nuclear Engineering and Design*, 268:203–214, 2014. doi: 10.1016/J.NUCENGDES.2013.04.046.

[52] X. Duan, B. Phillips, T. McKrell, and J. Buongiorno. Synchronized high-speed video, infrared thermometry, and particle image velocimetry data for validation of interface-tracking simulations of nucleate boiling phenomena. *Experimental Heat Transfer*, 26 (2-3):169–197, 2013. doi: 10.1080/08916152.2012.736837.

[53] V. Voulgaropoulos, G.M. Aguiar, O.K. Matar, M. Bucci, and C.N. Markides. Temperature and velocity field measurements of pool boiling using two-colour laser-induced

fluorescence, infrared thermometry and particle image velocimetry. In *10th International Conference on Multiphase Flow*, may 2019. URL `http://spiral.imperial.ac.uk/handle/10044/1/68411`.

[54] I. Zadrazil and C.N. Markides. An experimental characterization of liquid films in downwards co-current gas-liquid annular flow by particle image and tracking velocimetry. *International Journal of Multiphase Flow*, 67:42–53, 2014. doi: 10.1016/j.ijmultiphaseflow.2014.08.007.

[55] A. Charogiannis, J.S. An, and C.N. Markides. A simultaneous planar laser-induced fluorescence, particle image velocimetry and particle tracking velocimetry technique for the investigation of thin liquid-film flows. *Experimental Thermal and Fluid Science*, 68:516–536, 2015. doi: 10.1016/j.expthermflusci.2015.06.008.

[56] A.V. Cherdantsev, J.S. An, A. Charogiannis, and C.N. Markides. Simultaneous application of two laser-induced fluorescence approaches for film thickness measurements in annular gas-liquid flows. *International Journal of Multiphase Flow*, 119:237–258, 2019. doi: 10.1016/J.IJMULTIPHASEFLOW.2019.07.013.

[57] S.F. Wright, I. Zadrazil, and C.N. Markides. A review of solid–fluid selection options for optical-based measurements in single-phase liquid, two-phase liquid–liquid and multiphase solid–liquid flows. *Experiments in Fluids*, 58(9):1–39, 2017. doi: 10.1007/s00348-017-2386-y.

[58] R. Ibarra, I. Zadrazil, O.K. Matar, and C.N. Markides. Dynamics of liquid–liquid flows in horizontal pipes using simultaneous two–line planar laser–induced fluorescence and particle velocimetry. *International Journal of Multiphase Flow*, 101:47–63, 2018. doi: 10.1016/j.ijmultiphaseflow.2017.12.018.

[59] J.G. Collier and J.R. Thome. *Convective boiling and condensation*. Clarendon Press, 3 edition, 1994. ISBN 0198562969. doi: 10.1017/S0022112095233160.

[60] D. Steiner. H3. 1 flow patterns in evaporator tubes. *Verein Deutscher Ingenieure. VDI Heat Atlas:*, 2010.

[61] S. Z. Rouhani and E. Axelsson. Calculation of void volume fraction in the subcooled

and quality boiling regions. *International Journal of Heat and Mass Transfer*, 13(2): 383–393, 1970. doi: 10.1016/0017-9310(70)90114-6.

[62] I.H. Bell, J. Wronski, S. Quoilin, and V. Lemort. Pure and pseudo-pure fluid thermophysical property evaluation and the open-source thermophysical property library coolprop. *Industrial & Engineering Chemistry Research*, 53(6):2498–2508, 2014. doi: 10.1021/ie4033999. URL `http://pubs.acs.org/doi/abs/10.1021/ie4033999`.

[63] J.P. Meyer, M. Everts, N. Coetzee, K. Grote, and M. Steyn. Heat transfer coefficients of laminar, transitional, quasi-turbulent and turbulent flow in circular tubes. *International Communications in Heat and Mass Transfer*, 105:84–106, 2019. doi: 10.1016/j.icheatmasstransfer.2019.03.016.

[64] X. Fang, Y. Xu, and Z. Zhou. New correlations of single-phase friction factor for turbulent pipe flow and evaluation of existing single-phase friction factor correlations. *Nuclear Engineering and Design*, 241(3):897–902, 2011. doi: 10.1016/j.nucengdes.2010.12.019.

[65] .J. Moffat. Describing the uncertainties in experimental results. *Experimental Thermal and Fluid Science*, 1(1):3–17, 1988. doi: 10.1016/0894-1777(88)90043-X.

[66] D. Biberg. An explicit approximation for the wetted angle in two-Phase stratified pipe flow. *The Canadian Journal of Chemical Engineering*, 77(6):1221–1224, 1999. doi: 10.1002/cjce.5450770619.

[67] J. Garcia Pabon, A. Khosravi, R. Nunes, and L. Machado. Experimental investigation of pressure drop during two-phase flow of R1234yf in smooth horizontal tubes with internal diameters of 3.2 mm to 8.0 mm. *International Journal of Refrigeration*, 104: 426–436, 2019. doi: 10.1016/j.ijrefrig.2019.05.019.

[68] X. Fang, F. Zhuang, C. Chen, Q. Wu, Y. Chen, Y. Chen, and Yan He. Saturated flow boiling heat transfer: review and assessment of prediction methods. *Heat and Mass Transfer*, 55:197–222, 2019. doi: 10.1007/s00231-018-2432-1.

[69] L. Wojtan, T. Ursenbacher, and J.R. Thome. Investigation of flow boiling in horizontal tubes: Part II - Development of a new heat transfer model for stratified-wavy,

dryout and mist flow regimes. *International Journal of Heat and Mass Transfer*, 48 (14):2970–2985, 2005. doi: 10.1016/j.ijheatmasstransfer.2004.12.013.

[70] J.R. Thome, L. Cheng, G. Ribatski, and L.F. Vales. Flow boiling of ammonia and hydrocarbons: A state-of-the-art review. *International Journal of Refrigeration*, 31 (4):603–620, 2008. doi: 10.1016/J.IJREFRIG.2007.11.010.

[71] I. Mostinski. Application of the rule of corresponding states for calculation of heat transfer and critical heat flux. *Teploenergetika*, 4(4):66–71, 1963.

[72] M.G. Cooper. Heat flow rates in saturated nucleate pool boiling-A wide-ranging examination using reduced properties. *Advances in Heat Transfer*, 16(C):157–239, 1984. ISSN 00652717. doi: 10.1016/S0065-2717(08)70205-3.

[73] D. Gorenflo. Pool boiling. In *VDI Heat Atlas*. VDI-Verlag, Düsseldorf, Germany, 1993.

[74] G. Ribatski and J.M.S. Jabardo. Experimental study of nucleate boiling of halocarbon refrigerants on cylindrical surfaces. *International Journal of Heat and Mass Transfer*, 46(23):4439–4451, 2003. doi: 10.1016/S0017-9310(03)00252-7.

[75] D. Gorenflo and D. Kenning. Pool Boiling. In *VDI Heat Atlas*, chapter H2, pages 757–792. Springer Berlin Heidelberg, 2009. doi: 10.1007/978-3-540-77877-6_45.

[76] K. Stephan and M. Abdelsalam. Heat-transfer correlations for natural convection boiling. *International Journal of Heat and Mass Transfer*, 23(1):73–87, 1980. doi: 10.1016/0017-9310(80)90140-4.

[77] S. Halon, B. Gil, B. Bialko, and B. Zajaczkowski. Influence of saturation temperature and heat flux on pool boiling of R245fa. *Experimental Heat Transfer*, pages 1–18, 2020. doi: 10.1080/08916152.2020.1795009.

[78] D. Jung, Y. Kim, Y. Ko, and K. Song. Nucleate boiling heat transfer coefficients of pure halogenated refrigerants. *International Journal of Refrigeration*, 26:240–248, 2003. doi: 10.1016/S0140-7007(02)00040-3.

[79] W. Yao, D. Bestion, P. Coste, and M. Boucker. A three-dimensional two-fluid modeling of stratified flow with condensation for pressurized thermal shock investigations. *Nuclear Technology*, 152(1):129–142, 2005. doi: 10.13182/NT05-A3665.

[80] S.G. Yiantsios and B.G. Higgins. Linear stability of plane Poiseuille flow of two superposed fluids. *Physics of Fluids*, 31(11 , Nov. 1988):3225–3238, 1988. doi: 10.1063/1.866933.

[81] Z. Yang, M. Gong, G. Chen, X. Zou, and J. Shen. Two-phase flow patterns, heat transfer and pressure drop characteristics of R600a during flow boiling inside a horizontal tube. *Applied Thermal Engineering*, 120:654–671, 2017. doi: 10.1016/j.applthermaleng.2017.03.124.

[82] G. Lillo, R. Mastrullo, A.W. Mauro, and L. Viscito. Flow boiling of R32 in a horizontal stainless steel tube with 6.00 mm ID. Experiments, assessment of correlations and comparison with refrigerant R410A. *International Journal of Refrigeration*, 97:143–156, 2019. doi: 10.1016/j.ijrefrig.2018.09.024.

[83] C.N. Markides, R. Mathie, and A. Charogiannis. An experimental study of spatiotemporally resolved heat transfer in thin liquid-film flows falling over an inclined heated foil. *International Journal of Heat and Mass Transfer*, 93:872–888, 2016. doi: 10.1016/j.ijheatmasstransfer.2015.10.062. URL `http://dx.doi.org/10.1016/j.ijheatmasstransfer.2015.10.062`.

[84] J. Song, X. Li, K. Wang, and C.N. Markides. Parametric optimisation of a combined supercritical CO2 (S-CO2) cycle and organic Rankine cycle (ORC) system for internal combustion engine (ICE) waste-heat recovery. *Energy Conversion and Management*, 218:112999, 2020. doi: 10.1016/j.enconman.2020.112999.

[85] B.F. Tchanche, S. Quoilin, S. Declaye, G. Papadakis, and V. Lemort. Economic feasibility study of a small scale organic rankine cycle system in waste heat recovery application. In *ASME 2010 10th Biennial Conference on Engineering Systems Design and Analysis, ESDA2010*, volume 1, pages 249–256. American Society of Mechanical Engineers Digital Collection, 2010. doi: 10.1115/ESDA2010-24828.

[86] M.T. White, O.A. Oyewunmi, M.A. Chatzopoulou, A.M. Pantaleo, A.J. Haslam, and C.N. Markides. Computer-aided working-fluid design, thermodynamic optimisation and thermoeconomic assessment of ORC systems for waste-heat recovery. *Energy*, 161:1181–1198, 2018. doi: 10.1016/j.energy.2018.07.098.

[87] L.M.T. van Kleef, O.A. Oyewunmi, and C.N. Markides. Multi-objective thermo-economic optimization of organic Rankine cycle (ORC) power systems in waste-heat recovery applications using computer-aided molecular design techniques. *Applied Energy*, 251:112513, 2019. ISSN 03062619. doi: 10.1016/j.apenergy.2019.01.071.

[88] S.D. Odeh, M. Behnia, and G.L. Morrison. Hydrodynamic analysis of direct steam generation solar collectors. *Journal of Solar Energy Engineering*, 122(1):14, 2000. doi: 10.1115/1.556273.

[89] J.I. Ajona, U. Herrmann, F. Sperduto, and J. Farinha-Mendes. Main achievements within ARDISS (Advanced Receiver for Direct Solar Steam Production in Parabolic Trough Solar Power Plants) project. In Manfred Becker, editor, *Components, tools, facilities and measurement techniques. - (Solar thermal concentrating technologies : proceedings of the 8th international symposium, October, 6 - 11, 1996, Köln, Germany ; Vol. 2)*, pages 733–754, 1996.